ZEUS-prel-14-007
H1prelim-14-042
April 2014

QCD Analysis of the Inclusive $e^{\pm}p$ Scattering Cross Sections at HERA

H1 and ZEUS Collaborations

Abstract

The newly combined HERA-I and II data are input to QCD analyses at NLO and NNLO which determine preliminary versions of new sets of parton distributions, HERAPDF2.0(prel.), with small experimental uncertainties. Model and parametrisation uncertainties of the fits are also considered.

1 QCD Analysis of the Combined Data

The new combined data set on NC and CC e^+p and e^-p inclusive cross sections [1] is used as the input for next-to-leading order (NLO) and next-to next to leading order (NNLO) QCD PDF fits resulting in a new preliminary PDF set called HERAPDF2.0(prel.). The NC e^+p data includes data at different centre-of-mass energies such that different values of y are accessed at the same x, Q^2. This data set has 162 systematic uncertainties which result from the ZEUS and H1 data sets plus three sources of uncertainty which result from the combination procedure. All these sources are treated as correlated in the QCD fit. The Hessian method is used to evaluate the experimental uncertainties using the conventional χ^2 tolerance, $\Delta\chi^2 = 1$. The χ^2 definition is taken from ref. [2].

The QCD predictions for the structure functions are obtained by solving the DGLAP evolution equations [3–7] at NLO and NNLO in the $\overline{\text{MS}}$ scheme with the renormalisation and factorisation scales chosen to be Q^2. The program QCDNUM [8] is used within the HERAFitter framework [9]. The DGLAP equations yield the PDFs at all values of Q^2 if they are provided as functions of Bjorken-x at some input scale Q_0^2. This scale is chosen to be $Q_0^2 = 1.9$ GeV^2 as for HERAPDF1.0 [10]. The light quark coefficient functions are calculated in QCDNUM. The heavy quark coefficient functions are calculated in the general-mass variable-flavour-number scheme of [11], with recent modifications [12,14]- called RTOPT. The charm quark mass parameter M_c in this scheme, M_c^{opt} , is determined by performing a χ^2-scan vs. M_c of these new inclusive data together with the HERA combined charm data [13] following the procedure outlined in that paper. The value of the charm mass parameter is thus determined to be $M_c^{opt} = 1.47$ GeV for the NLO fits and $M_c^{opt} = 1.44$ GeV for the NNLO fits. The beauty quark mass parameter is chosen as $M_b = 4.75$ GeV following [16]. The strong coupling constant is fixed to the value $\alpha_s(M_Z^2) = 0.118$ [15] for both the NLO and NNLO fits.

1.1 Parametrisations

PDFs are parametrised as a function of Bjorken-x at the input scale by the generic form

$$xf(x) = Ax^B(1-x)^C(1+Dx+Ex^2). \quad (1)$$

with the exception of the gluon for which an additional term of the form [1] $A'_g x^{B'_g}(1-x)^{C'_g}$ is subtracted. The parametrised PDFs are the gluon distribution xg, the valence quark distributions xu_v, xd_v, and the u-type and d-type anti-quark distributions $x\bar{U}$, $x\bar{D}$. Here $x\bar{U} = x\bar{u}$, $x\bar{D} = x\bar{d}+x\bar{s}$ at the chosen starting scale. The central fit is found by first setting the D, E and A'_g parameters to zero (this leaves 10 parameters free) and then introducing them into the fit one at a time until the fit χ^2 saturates. This results in a 15 parameter fit which satisfies the criteria that all the PDFs are positive and all predicted cross sections are positive in the fitted region.

[1] $C'_g = 25$ is fixed since the fit is not sensitive to this value provided it is high enough ($C'_g > 15$) that the term does not contribute at large x.

The resulting parametrisations are

$$xg(x) = A_g x^{B_g}(1-x)^{C_g} - A'_g x^{B'_g}(1-x)^{C'_g}, \quad (2)$$

$$xu_v(x) = A_{u_v} x^{B_{u_v}}(1-x)^{C_{u_v}}\left(1 + D_{u_v}x + E_{u_v}x^2\right), \quad (3)$$

$$xd_v(x) = A_{d_v} x^{B_{d_v}}(1-x)^{C_{d_v}}, \quad (4)$$

$$x\bar{U}(x) = A_{\bar{U}} x^{B_{\bar{U}}}(1-x)^{C_{\bar{U}}}\left(1 + D_{\bar{U}}x\right), \quad (5)$$

$$x\bar{D}(x) = A_{\bar{D}} x^{B_{\bar{D}}}(1-x)^{C_{\bar{D}}}. \quad (6)$$

The normalisation parameters, A_g, A_{u_v}, A_{d_v}, are constrained by the quark number sum rules and momentum sum rule. The B parameters $B_{\bar{U}}$ and $B_{\bar{D}}$ are set equal, $B_{\bar{U}} = B_{\bar{D}}$, such that there is a single B parameter for the sea distributions. The strange quark distribution is expressed as x-independent fraction, f_s, of the d-type sea, $x\bar{s} = f_s x\bar{D}$ at Q_0^2. The central value $f_s = 0.4$ is chosen to be a compromise between the determination of a suppressed strange sea from neutrino-induced di-muon production [16,17] and a recent determination of an unsuppressed strange sea from the ATLAS collaboration [18]. The further constraint $A_{\bar{U}} = A_{\bar{D}}(1-f_s)$, together with the requirement $B_{\bar{U}} = B_{\bar{D}}$, ensures that $x\bar{u} \to x\bar{d}$ as $x \to 0$.

The HERA data used in the combination have a minimum invariant mass of the hadronic system, W, of 15 GeV and a maximum x of 0.65, such that they are in a kinematic region where there is no sensitivity to target mass and large-x higher-twist contributions. A minimum Q^2 cut of $Q^2_{min} = 3.5$ GeV^2 has been imposed on previous HERAPDF fits to remain in the kinematic region where perturbative QCD should be applicable. In the present analysis the value used for this cut is re-examined.

The predictions of the NLO and NNLO fits are first shown compared to the data using the standard cut $Q^2_{min} = 3.5$ GeV^2. Figs. 1, 2 show comparisons of the NLO and NNLO fits to low-Q^2 NC e^+p data for $\sqrt{s} = 318$ GeV. Figs. 3, 4 show comparisons of the NLO and NNLO fits to low-Q^2 NC e^+p data for $\sqrt{s} = 251$ GeV. Figs. 5, 6, show comparisons of the NLO and NNLO fits to low-Q^2 NC e^+p data for $\sqrt{s} = 225$ GeV.

Figs. 7, 8 show comparisons of the NLO and NNLO fits to high-Q^2 NC e^+p data for $\sqrt{s} = 318$ GeV. Figs. 9, 10, show comparisons of the NLO and NNLO fits to high-Q^2 NC e^+p data for $\sqrt{s} = 251$ GeV. Figs. 11, 12 show comparisons of the NLO and NNLO fits to high-Q^2 NC e^+p data for $\sqrt{s} = 225$ GeV.

Figs. 13, 14 show comparisons of the NLO and NNLO fits to high-Q^2 NC e^-p data for $\sqrt{s} = 318$ GeV. Figs. 15, 16 show comparisons of the NLO and NNLO fits to high-Q^2 NC e^-p and NC e^+p data for $\sqrt{s} = 318$ GeV.

Figs. 17, 18 show comparisons of the NLO and NNLO fits to high-Q^2 CC e^+p data for $\sqrt{s} = 318$ GeV. Figs. 19, 20 show comparisons of the NLO and NNLO fits to high-Q^2 CCe e^-p data for $\sqrt{s} = 318$ GeV.

Figs. 21, 22 show comparisons of the NLO and NNLO fits to NC e^+p data from HERA and to fixed target data.

Fig.23 shows the NC e^+p data for very low Q^2, below the fitted region, and is included for completeness.

For the kinematic cut $Q^2_{min} = 3.5$ GeV^2 the χ^2 per degree of freedom for the central NLO fit is 1385/1130 and for the central NNLO fit it is 1414/1130. These values are somewhat larger than

Variation	Standard Value	Lower Limit	Upper Limit
f_s	0.4	0.3	0.5
M_c^{opt}(NLO) [GeV]	1.47	1.41	1.53
M_c^{opt} (NNLO) [GeV]	1.44	1.38	1.50
M_b [GeV]	4.75	4.5	5.0
Q^2_{min} [GeV^2]	10.0	7.5	12.5
Q^2_{min} [GeV^2]	3.5	2.5	5.0
Q^2_0 [GeV^2]	1.9	1.6	2.2

Table 1: Standard values of input parameters and the variations considered.

for HERAPDF1.0 and thus we examine the dependence of the χ^2 on the Q^2 cut applied to the data. Fig. 24 shows scans of χ^2 per degree of freedom vs the minimum Q^2_{min} of data used in the fit for the NLO QCD fit and the NNLO QCD fits. The values drop steadily until $Q^2_{min} \sim 10$ GeV^2, when χ^2 per degree of freedom is 1156/1003 for NLO and 1150/1003 at NNLO. Thus fits are presented for $Q^2_{min} = 10$ GeV^2 as well as for our standard cut $Q^2_{min} = 3.5$ GeV^2.

In Figures 25 and 26 the fit predictions are compared to low-Q^2 NC e^+p data at $\sqrt{s} = 318$ GeV for NLO and NNLO fits for which $Q^2_{min} = 10$ GeV^2. The data for $Q^2 < 10$GeV^2 are poorly described since they are not in the fit, but more signficantly the discrepancies from the fit predictions (shown by dashed lines for data that are not used in the fit) show a systematic trend becoming larger for lower x and lower Q^2. The description of these low-x, low-Q^2 data is not improved at NNLO.

1.2 Model and Parametrisation Uncertainties

Model uncertainties and parametrisation uncertainties of the central fit solution are evaluated by varying the input assumptions. The variation of numerical values chosen for the central fit is specified in Table 1. The variation of f_s is chosen to span the ranges between a suppressed strange sea as determined in [16,17] and an unsuppressed strange sea [18]. The variation of M_c^{opt} is taken from the χ^2-scan vs. M_c for the RTOPT heavy quark scheme following the procedure outline in ref. [13]. This allows a considerably reduced uncertainty due to M_c variation as compared to the HERAPDF1.0 analysis. The variation of M_b is taken from reference [16].

The difference between the central fit and the fits corresponding to model variations of M_c, M_b, f_s, Q^2_{min} are added in quadrature, separately for positive and negative deviations, and represent the model uncertainty of the HERAPDF2.0(prel.) set.

The variation in Q^2_0 is regarded as a parametrisation uncertainty, rather than a model uncertainty. Variation of the number of terms in the polynomial $(1 + Dx + Ex^2)$ is also considered for each fitted parton distribution. All the 16 parameter fits which have one more D or E parameter non-zero are considered as possible variants. In practice none of these have significantly different PDF shapes from the central fit.

The difference between the parametrisation variations and the central fit is stored and an envelope representing the maximal deviation at each x value is constructed to represent the parametrisation uncertainty. This parametrisation uncertainty should be regarded as indicative

rather than exhaustive. The total PDF uncertainty is obtained by adding in quadrature experimental, model and parametrisation uncertainties.

In summary, the preliminary HERAPDF2.0 analysis uses a consistent data set with small correlated systematic uncertainties and applies the conventional χ^2 tolerance, $\Delta\chi^2 = 1$, when determining the experimental uncertainties on the PDFs. This data set includes four different processes, NC and CC, e^+p and e^-p scattering, such that there is sufficient information to extract $x\bar{U}$, $x\bar{D}$, xd_v, xu_v PDFs and the gluon PDF from the scaling violations. The NC e^+p data includes data at different centre-of-mass energies such that different values of y are accessed at the same x, Q^2. This makes the data sensitive to F_L and thus gives further information on the low-x gluon distribution.

1.3 Fit Results

Figs. 27 shows summary plots of the HERAPDF2.0(prel.) NLO fit for both values of Q^2_{min}, at the scale $\mu_f^2 = 10$ GeV^2. The experimental, model and parametrisation uncertainties are shown separately. The model and parameterisation uncertainties are asymmetric. For the sea and gluon distributions the uncertainties arising from the variation of Q^2_{min} affect the small-x region.

Figs. 28 compares the $Q^2_{min} = 3.5$GeV^2 NLO fit to the HERAPDF1.0 NLO on log and linear x scales. A considerable decrease in uncertainty can be observed, particularly in the high-x sea PDFs. The shapes of the PDFs have also changed somewhat. The valence shapes change due to the considerable increase high-x data. The high-x sea becomes softer and the high-x gluon becomes harder.

Figs. 29 compares the NLO $Q^2_{min} = 3.5$ GeV^2 fit to the $Q^2_{min} = 10$ GeV^2 fit on log and linear scales. There is a slight flattening of the low-x gluon and sea shapes for the $Q^2_{min} = 10$GeV^2 fit, but the main difference is an increase of low-x uncertainty.

Figs. 30 shows summary plots of the HERAPDF2.0(prel.) NNLO fit for both values of Q^2_{min} at $Q^2 = 10$ GeV^2. In this case there is very a signficant difference in low-x shape for these two fits. The choice of the value of Q^2_{min} shifts the gluon shape systematically towards becoming more valence-like and the sea shape towards becoming flatter.

Figs. 31 compares the $Q^2_{min} = 3.5$ GeV^2 NNLO fit to the HERAPDF1.5NNLO on log and linear x scales respectively. There is some further reduction in uncertainty, since the new combination contains more data at high-x than the preliminary HERA-I+II combination on which HERAPDF1.5 was based.

Figs. 32 compares the NNLO $Q^2_{min} = 3.5$ GeV^2 fit to the $Q^2_{min} = 10$ GeV^2 fit on log and linear scales. The shape of both the low-x sea and gluon differs systematically for these fits.

2 Conclusions

QCD analyses are performed at NLO and NNLO based exclusively on the newly combined HERA-I+II $e^\pm p$ scattering cross-section data. A new set of parton distribution functions, HERAPDF2.0(prel.), is obtained using a variable-flavour-number scheme. The analysis yields small experimental uncertainties and includes estimates for model and parametrisation uncertainties.

Acknowledgements

We are grateful to the HERA machine group whose outstanding efforts have made these experiments possible. We appreciate the contributions to the construction and maintenance of the H1 and ZEUS detectors of many people who are not listed as authors. We thank our funding agencies for financial support, the DESY technical staff for continuous assistance and the DESY directorate for their support and for the hospitality they extended to the non-DESY members of the collaborations.

References

[1] H1-prelim. **14-042**, ZEUS-prel. **007**, (2014).

[2] F. D. Aaron *et al* , JHEP **09**, 061 (2012).

[3] V. N. Gribov and L. N. Lipatov, Sov. J. Nucl. Phys. **15**, 438 (1972).

[4] V. N. Gribov and L. N. Lipatov, Sov. J. Nucl. Phys. **15**, 675 (1972).

[5] L. N. Lipatov, Sov. J. Nucl. Phys. **20**, 94 (1975).

[6] Y. L. Dokshitzer, Sov. Phys. JETP **46**, 641 (1977).

[7] G. Altarelli and G. Parisi, Nucl. Phys. B **126**, 298 (1977).

[8] M. Botje, Eur. Phys. J. **C14**, 285 (2000).

[9] http://herafitter.org, (2013).

[10] F. D. Aaron *et al* , JHEP **01**, 109 (2010).

[11] R. S. Thorne and R. G. Roberts, Phys. Rev. D **57**, 6871 (1998).

[12] R. S. Thorne, Phys. Rev. **D73**, 054019 (2006).

[13] F. D. Aaron *et al*, Eur. Phys. J **C73**, 2311 (2013).

[14] R. S. Thorne, private communication, 2012.

[15] J. Beringet *et al*, Phys. Rev. **D86**, 010001 (2012).

[16] A. D. Martin, W. J. Stirling, R. S. Thorne, and G. Watt (2009).

[17] P. M. Nadolsky *et al.*, Phys. Rev. **D78**, 013004 (2008).

[18] G Aad *et al*, Phys. Rev. Lett. **109**, 012001 (2012).

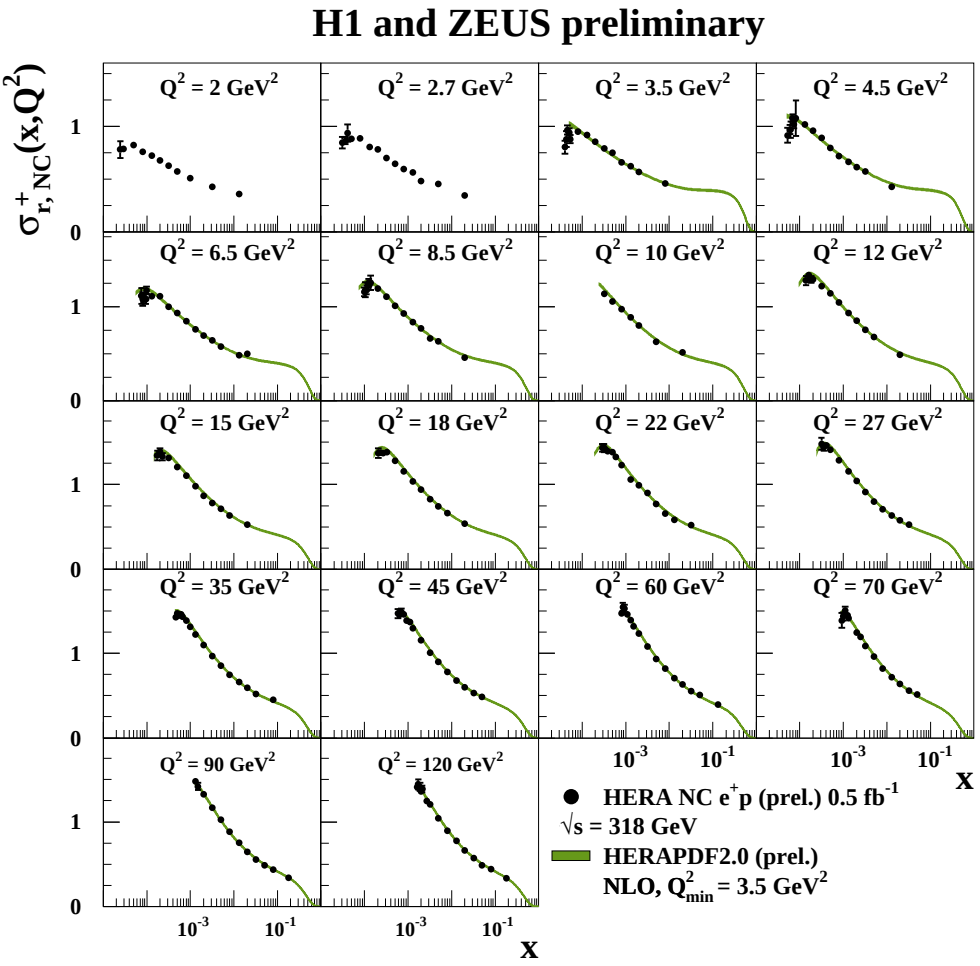

Figure 1: The combined low-Q^2 HERA data for the inclusive NC e^+p reduced cross section at $\sqrt{s}$ = 318 GeV compared to an NLO QCD fit with Q^2_{min} = 3.5 GeV^2. The green band includes experimental uncertainties on the fit.

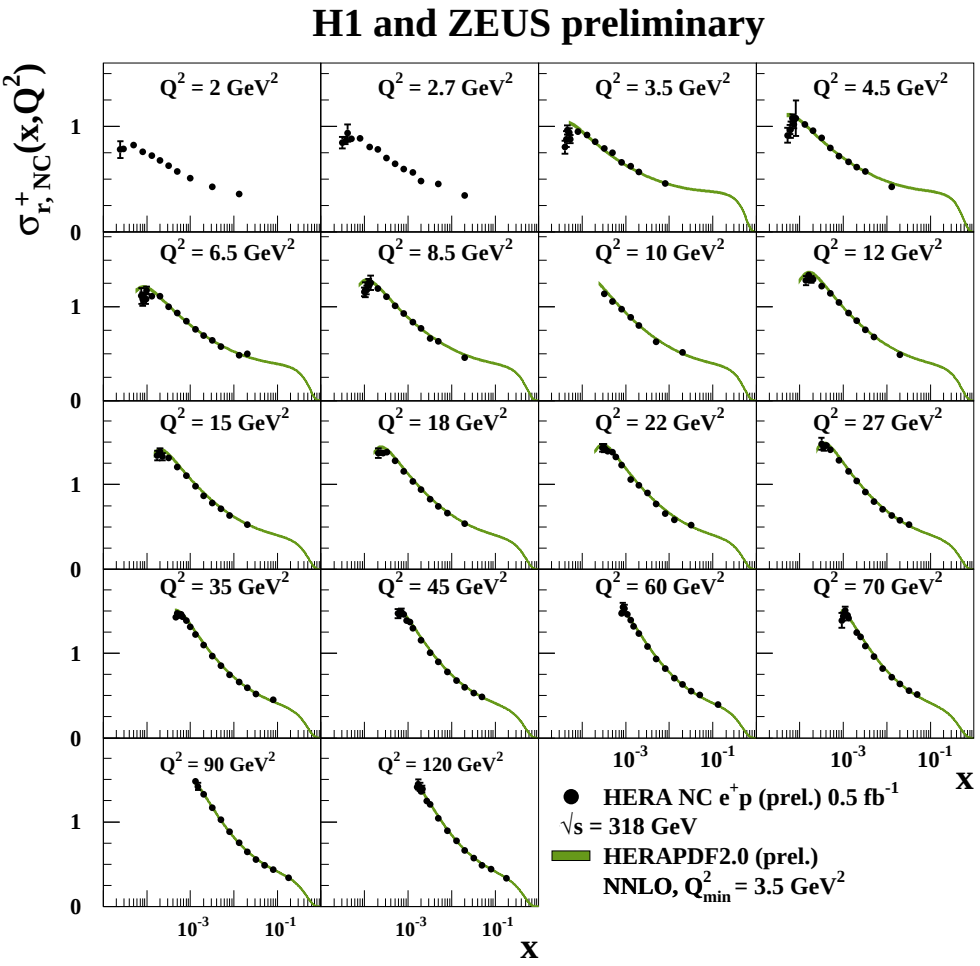

Figure 2: The combined low-Q^2 HERA data for the inclusive NC e^+p reduced cross section at $\sqrt{s}$ = 318 GeV compared to an NNLO QCD fit with Q^2_{min} = 3.5 GeV^2. The green band includes experimental uncertainties on the fit.

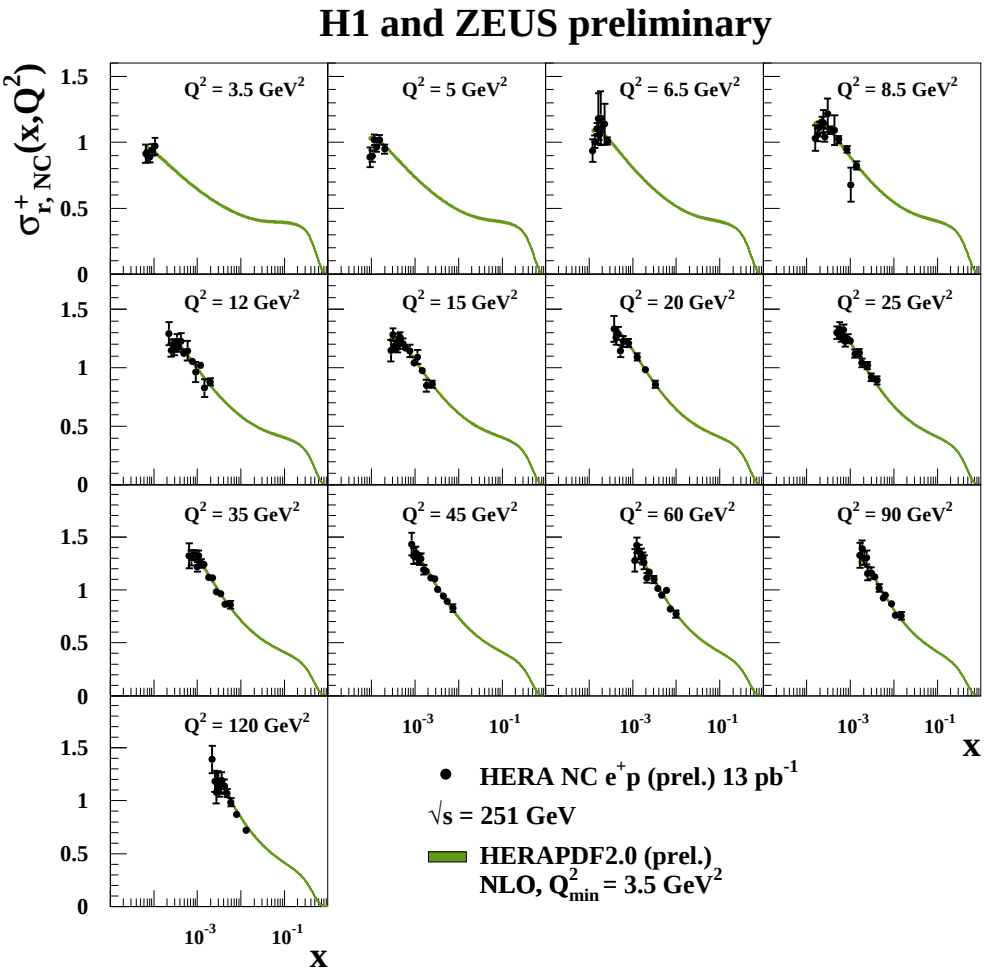

Figure 3: The combined low-Q^2 HERA data for the inclusive NC e^+p reduced cross section at $\sqrt{s}$ = 251 GeV compared to an NLO QCD fit with Q^2_{min} = 3.5 GeV^2. The green band includes experimental uncertainties on the fit.

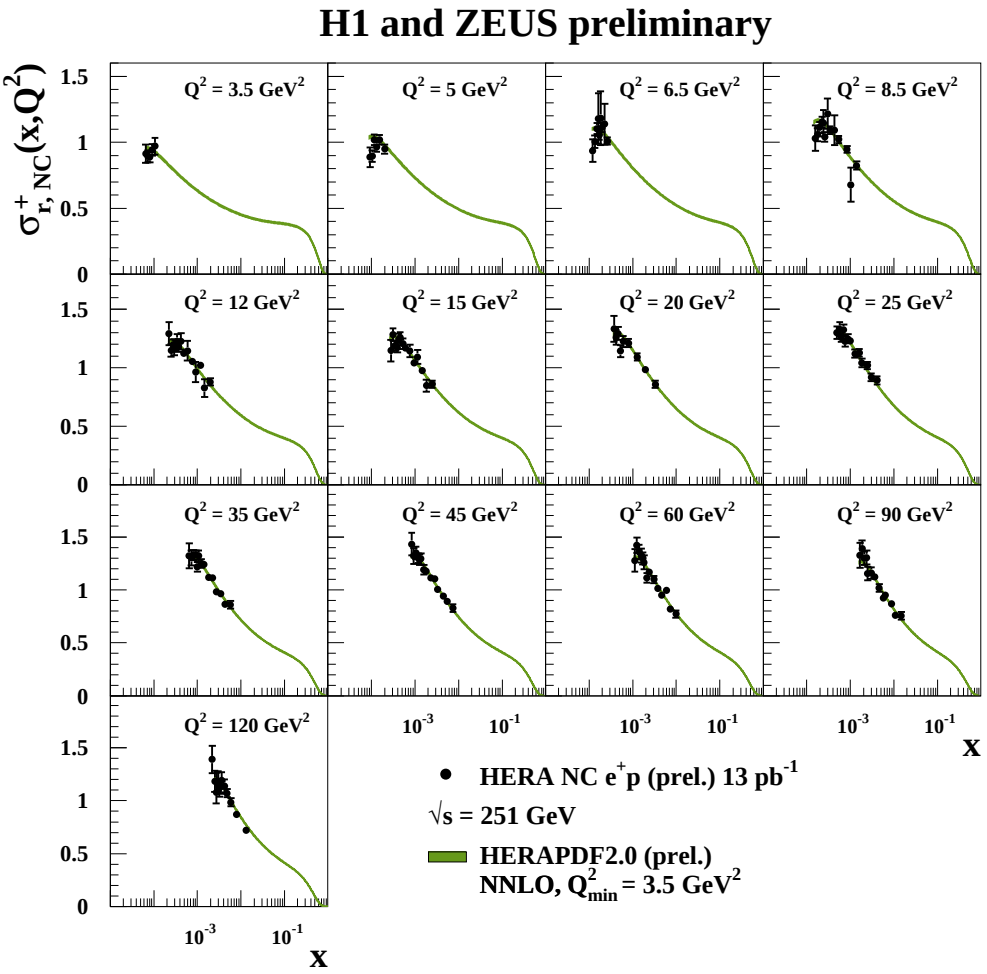

Figure 4: The combined low-Q^2 HERA data for the inclusive NC e^+p reduced cross section at $\sqrt{s}$ = 251 GeV compared to an NNLO QCD fit with Q^2_{min} = 3.5 GeV^2. The green band includes experimental uncertainties on the fit.

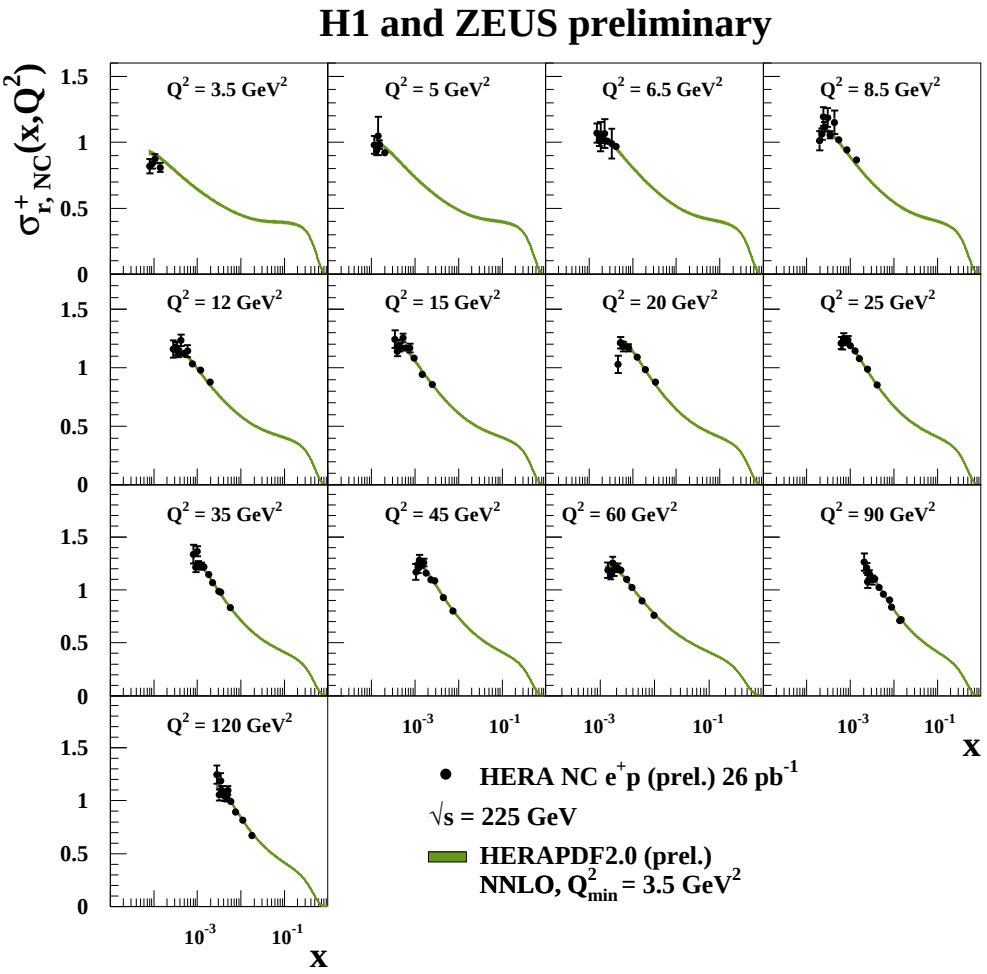

Figure 5: The combined low-Q^2 HERA data for the inclusive NC e^+p reduced cross section at $\sqrt{s}$ = 225 GeV compared to an NLO QCD fit with Q^2_{min} = 3.5 GeV^2. The green band includes experimental uncertainties on the fit.

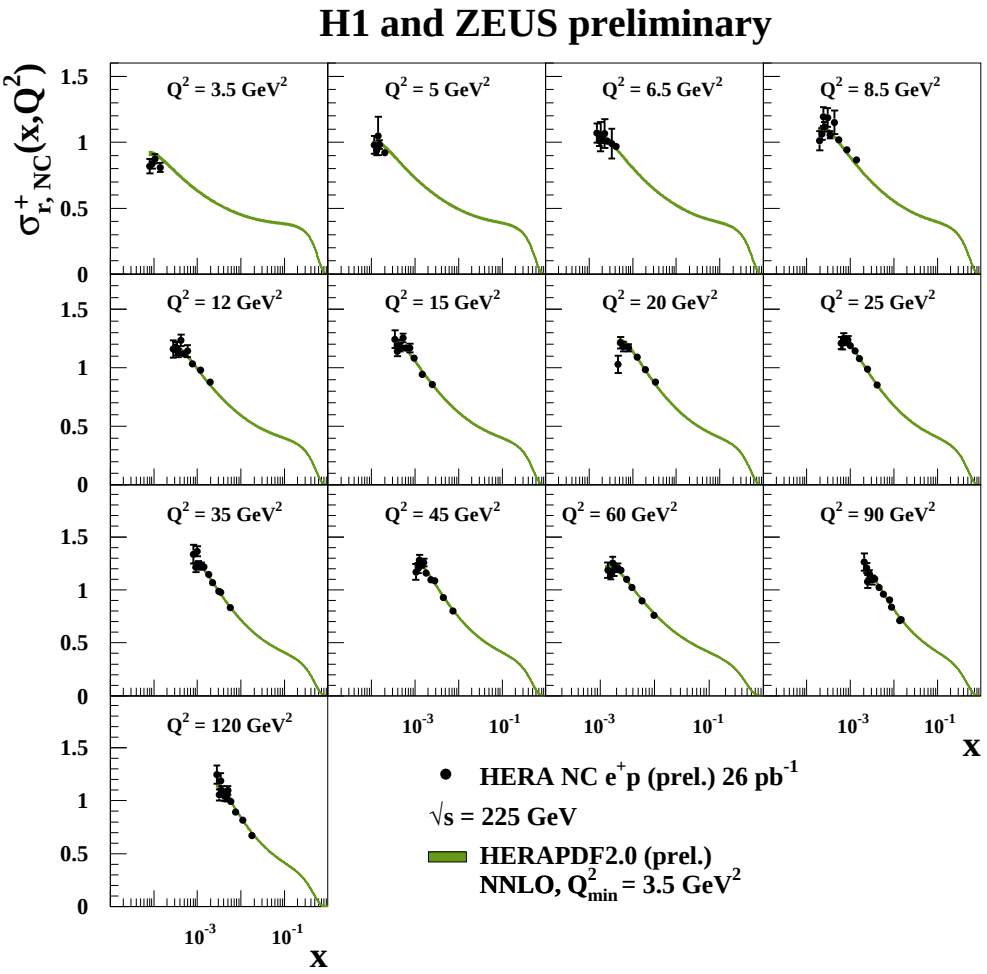

Figure 6: The combined low-Q^2 HERA data for the inclusive NC e^+p reduced cross section at $\sqrt{s}$ = 225 GeV compared to an NNLO QCD fit with Q^2_{min} = 3.5 GeV^2. The green band includes experimental uncertainties on the fit.

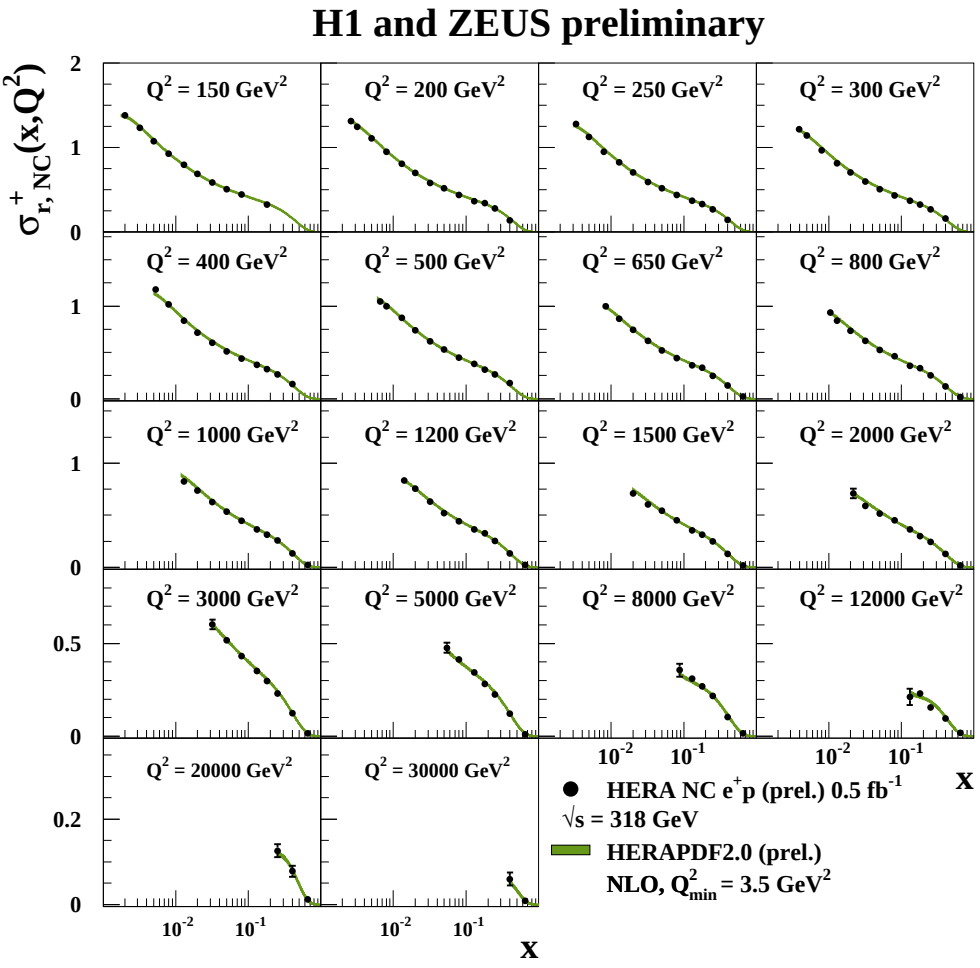

Figure 7: The combined high-Q^2 HERA data for the inclusive NC e^+p reduced cross section at $\sqrt{s}$ = 318 GeV compared to an NLO QCD fit with Q^2_{min} = 3.5 GeV^2. The green band includes experimental uncertainties on the fit.

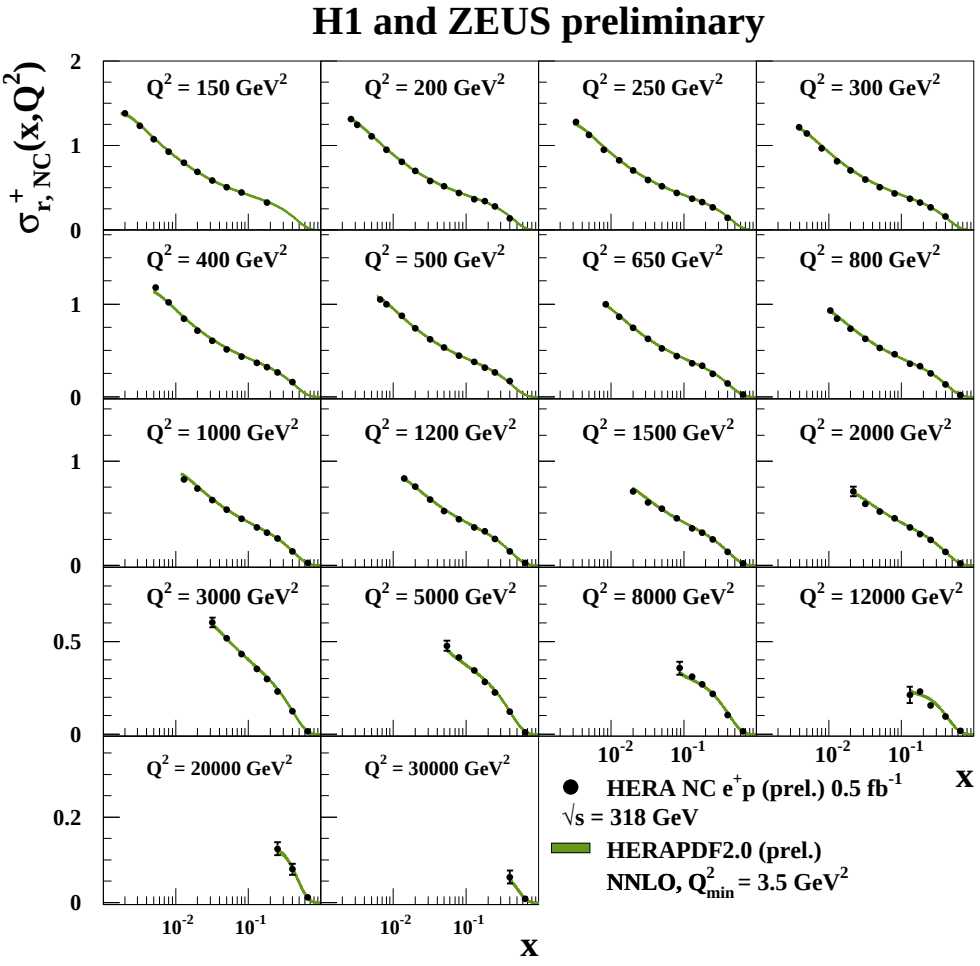

Figure 8: The combined high-Q^2 HERA data for the inclusive NC e^+p reduced cross section at $\sqrt{s}$ = 318 GeV compared to an NNLO QCD fit with Q^2_{min} = 3.5 GeV^2. The green band includes experimental uncertainties on the fit.

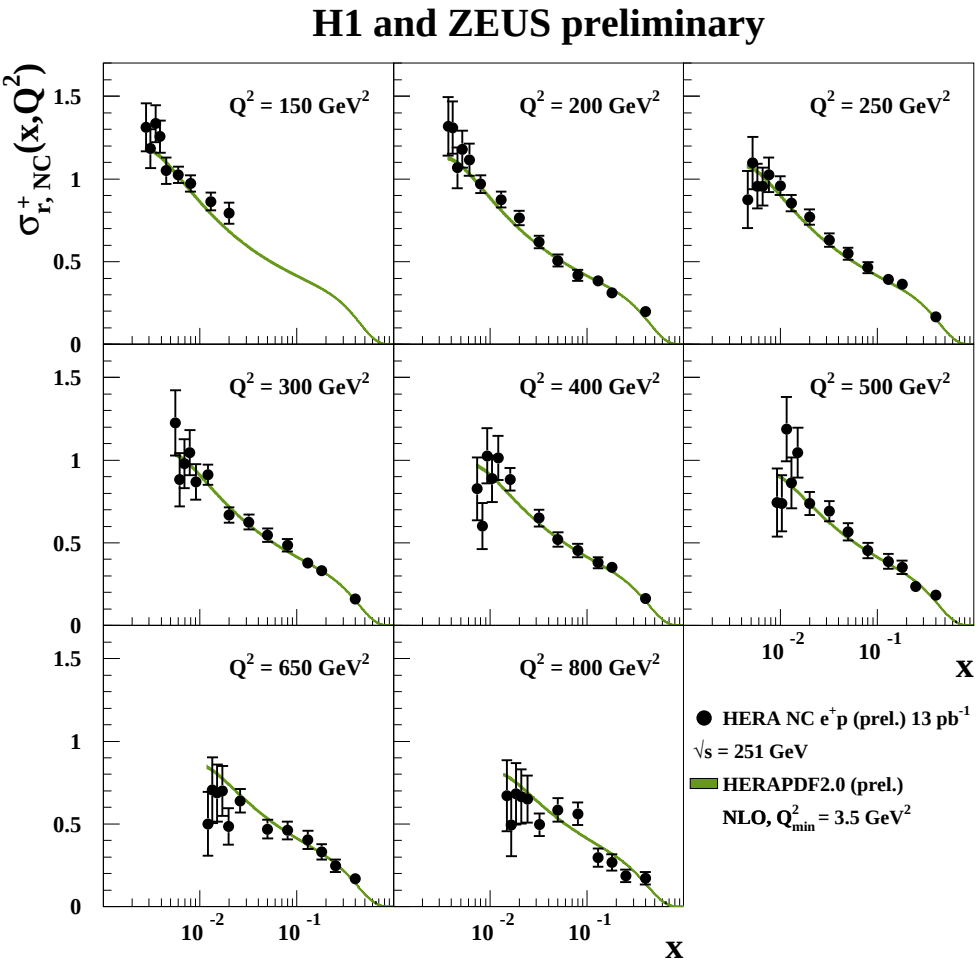

Figure 9: The combined high-Q^2 HERA data for the inclusive NC e^+p reduced cross section at $\sqrt{s}$ = 251 GeV compared to an NLO QCD fit with Q^2_{min} = 3.5 GeV^2. The green band includes experimental uncertainties on the fit.

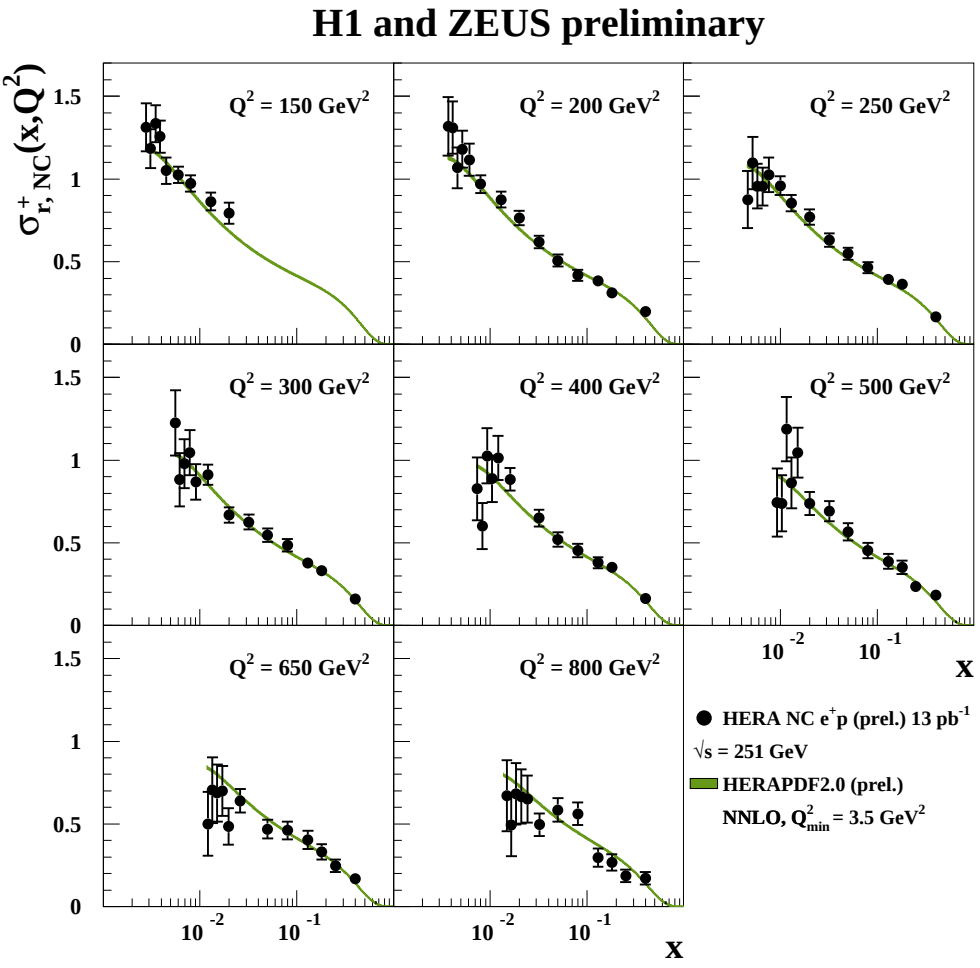

Figure 10: The combined high-Q^2 HERA data for the inclusive NC e^+p reduced cross section at $\sqrt{s} = 251$ GeV compared to an NNLO QCD fit with $Q^2_{min} = 3.5$ GeV^2. The green band includes experimental uncertainties on the fit.

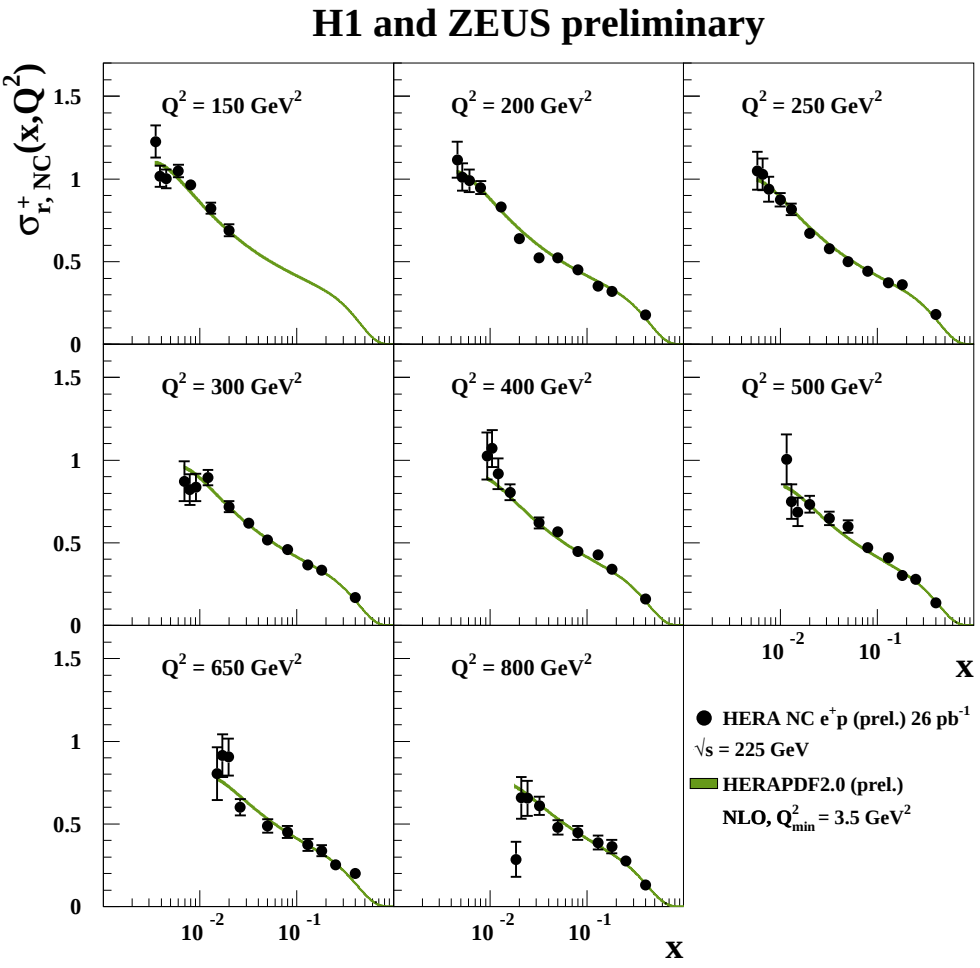

Figure 11: The combined high-Q^2 HERA data for the inclusive NC e^+p reduced cross section at $\sqrt{s}$ = 225 GeV compared to an NLO QCD fit with Q^2_{min} = 3.5 GeV^2. The green band includes experimental uncertainties on the fit.

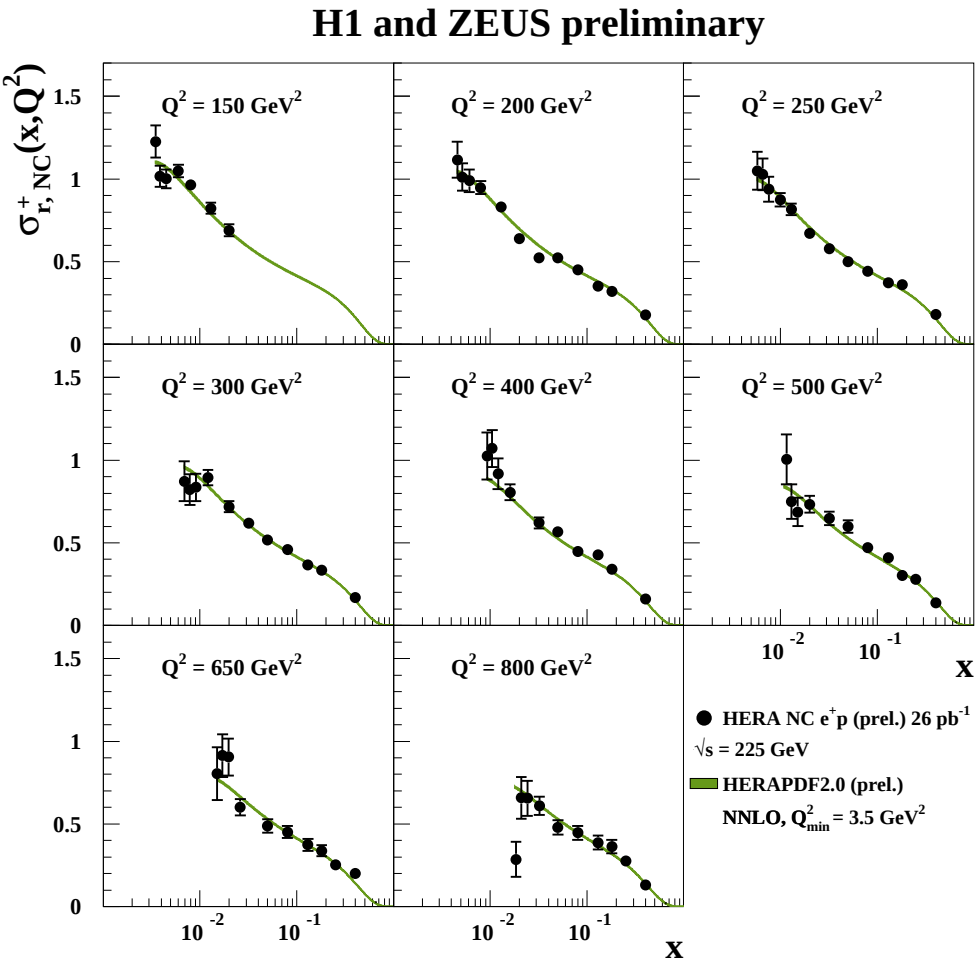

Figure 12: The combined high-Q^2 HERA data for the inclusive NC e^+p reduced cross section at $\sqrt{s} = 225$ GeV compared to an NNLO QCD fit with $Q^2_{min} = 3.5$ GeV^2. The green band includes experimental uncertainties on the fit.

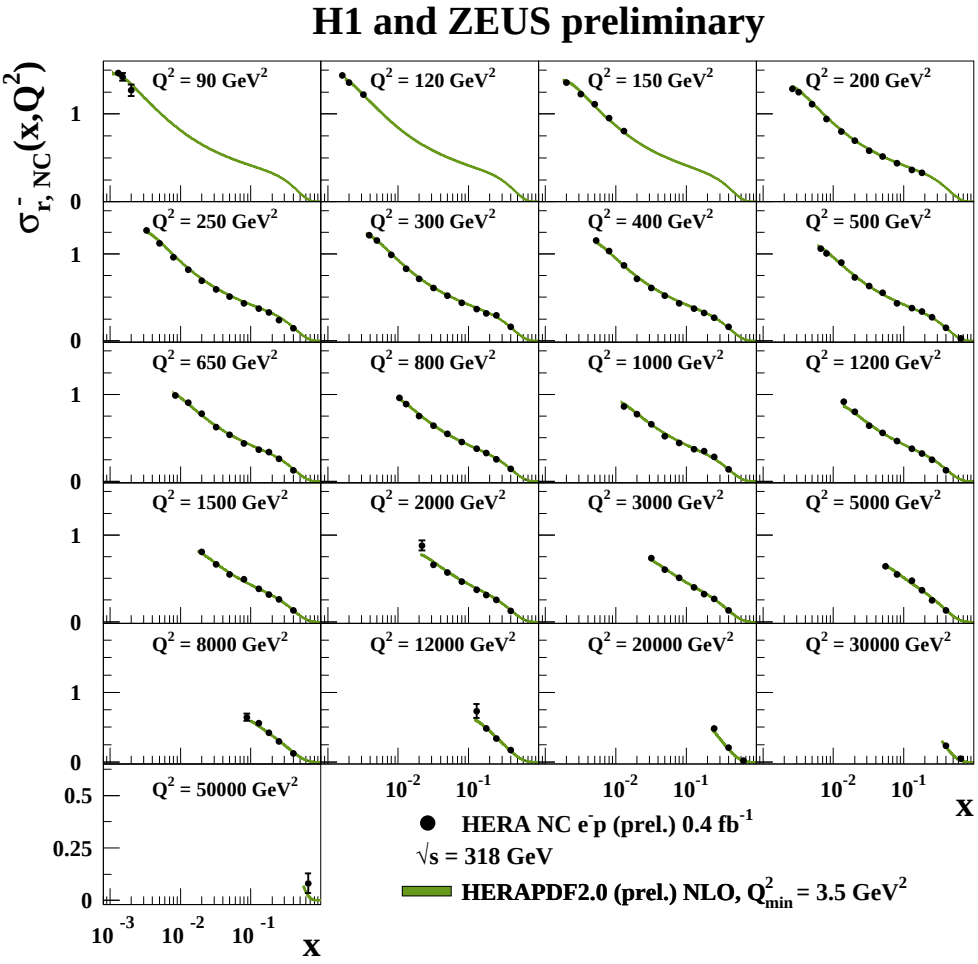

Figure 13: The combined HERA data for the inclusive NC $e^- p$ reduced cross section at $\sqrt{s}$ = 318 GeV compared to an NLO QCD fit with Q^2_{min} = 3.5 GeV^2. The green band includes experimental uncertainties on the fit.

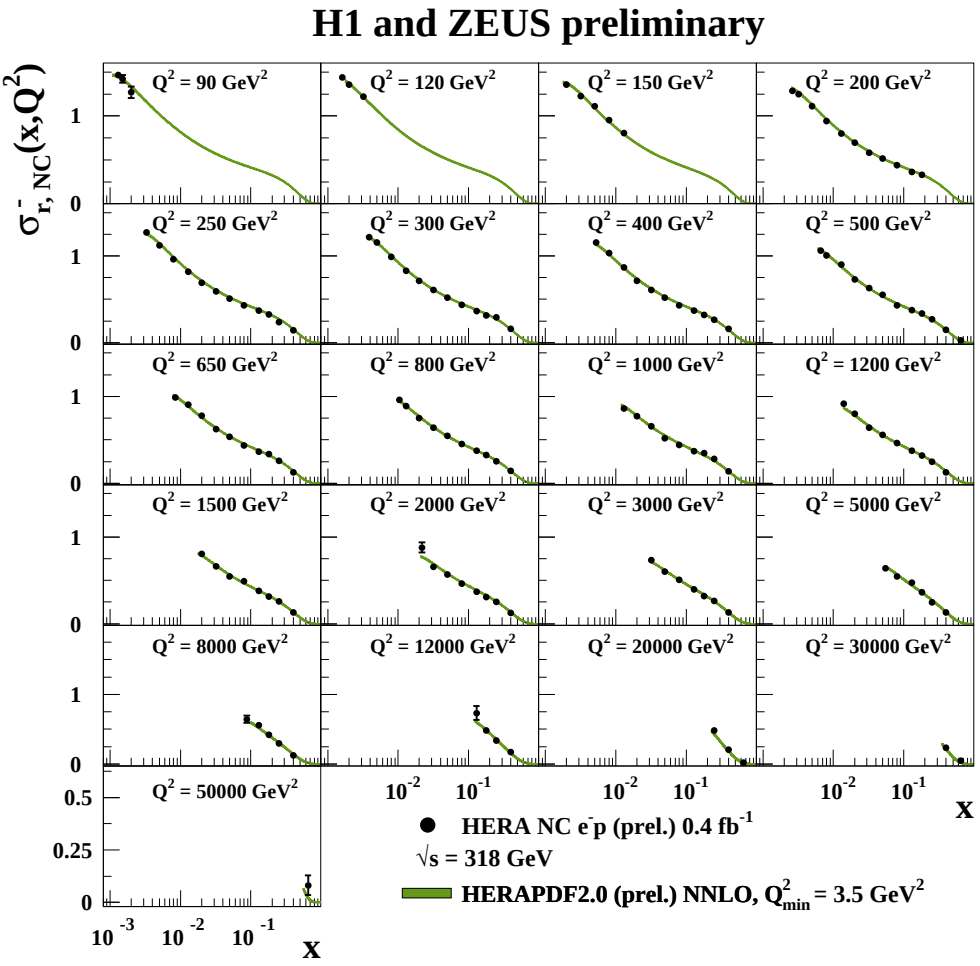

Figure 14: The combined HERA data for the inclusive NC $e^- p$ reduced cross section at $\sqrt{s}$ = 318 GeV compared to an NNLO QCD fit with Q^2_{min} = 3.5 GeV^2. The green band includes experimental uncertainties on the fit.

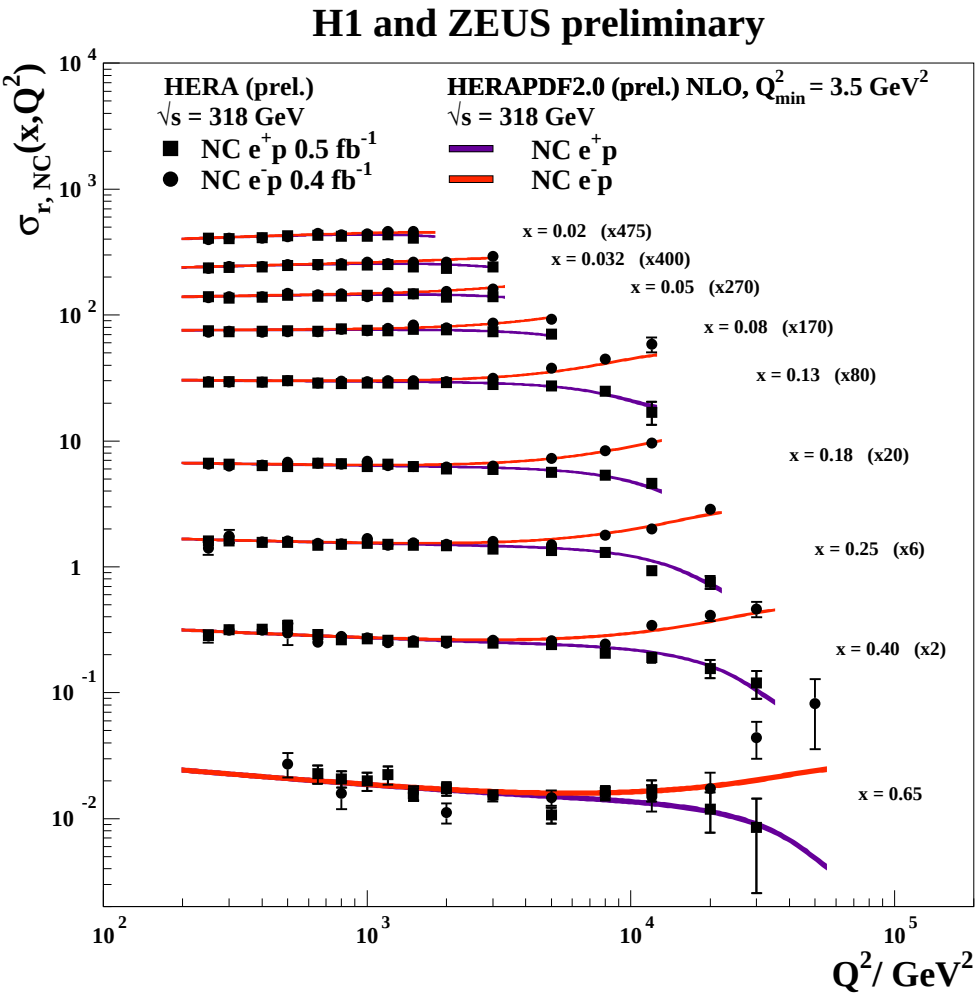

Figure 15: The combined HERA data for the inclusive NC $e^- p$ and $e^+ p$ reduced cross section at $\sqrt{s} = 318$ GeV compared to an NLO QCD fit with $Q^2_{min} = 3.5$ GeV^2. The green band includes experimental uncertainties on the fit.

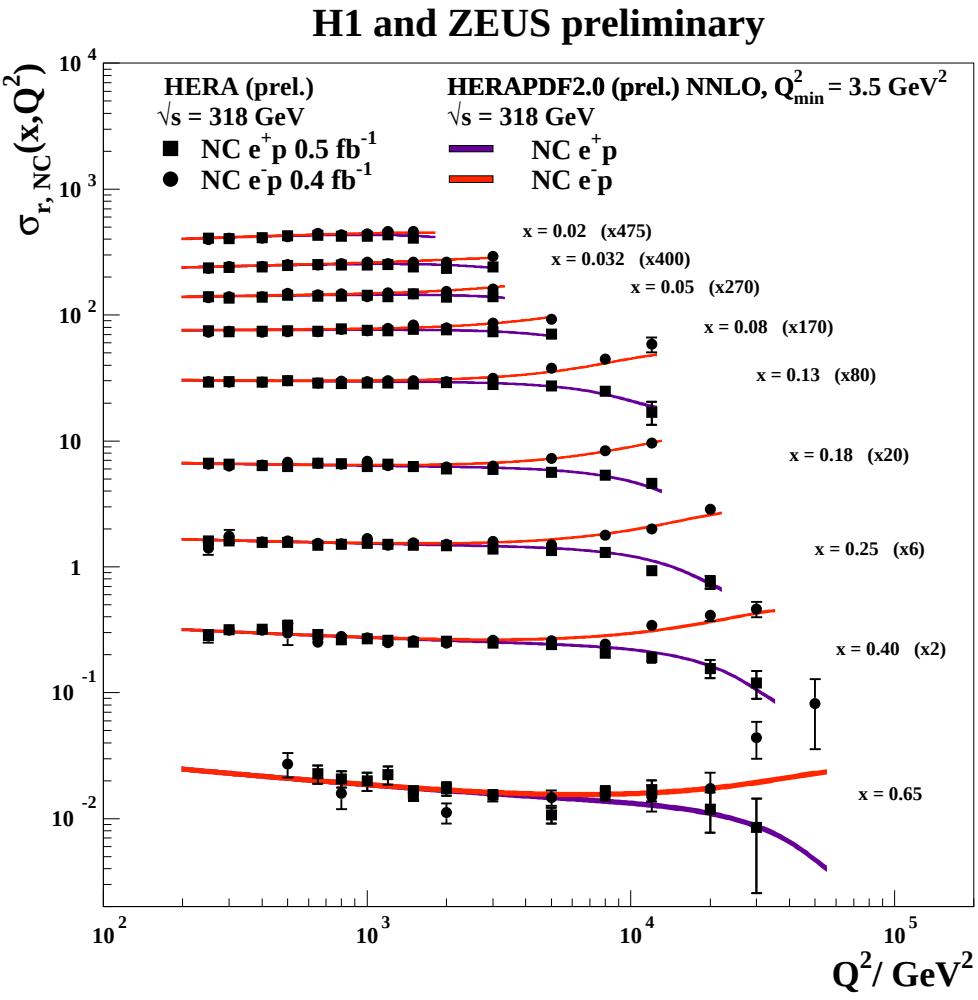

Figure 16: The combined HERA data for the inclusive NC $e^- p$ and $e^+ p$ reduced cross section at $\sqrt{s} = 318$ GeV compared to an NNLO QCD fit with $Q^2_{min} = 3.5$ GeV^2. The green band includes experimental uncertainties on the fit.

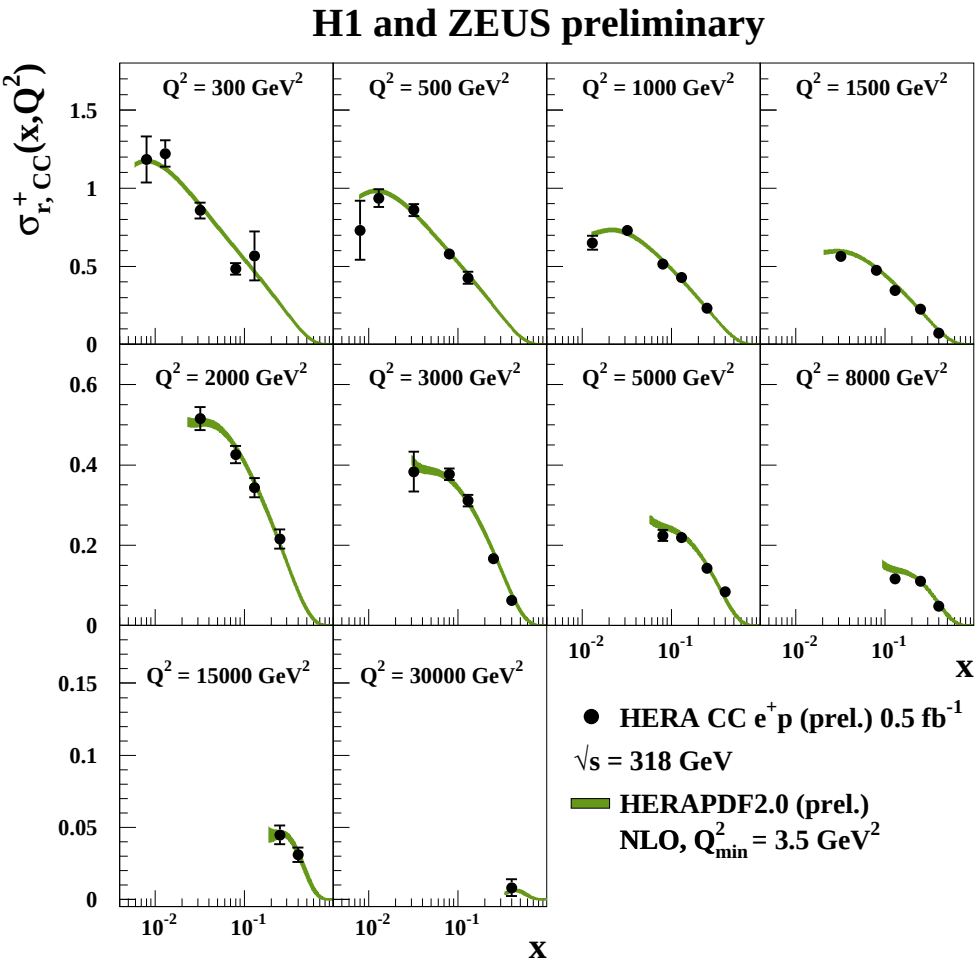

Figure 17: The combined HERA data for the inclusive CC e^+p reduced cross section at $\sqrt{s}$ = 318 GeV compared to an NLO QCD fit with Q^2_{min} = 3.5 GeV^2. The green band includes experimental uncertainties on the fit.

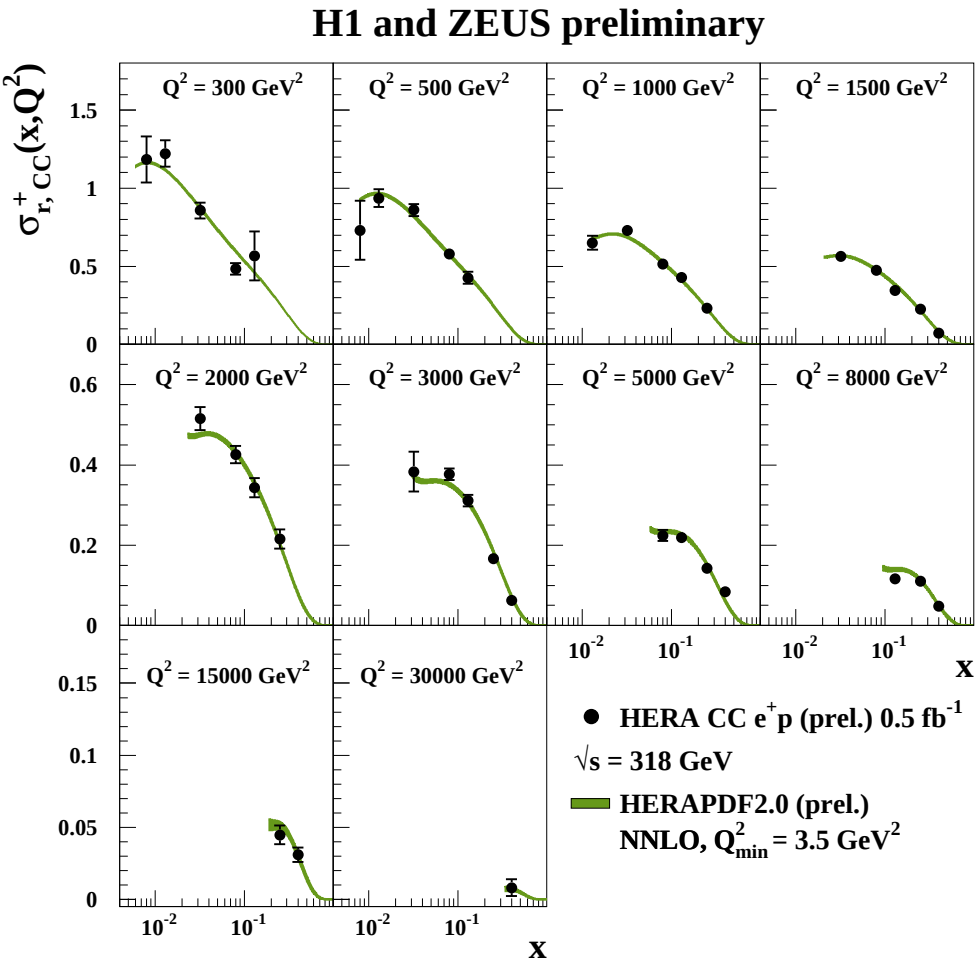

Figure 18: The combined HERA data for the inclusive CC e^+p reduced cross section at $\sqrt{s}$ = 318 GeV compared to an NNLO QCD fit with Q^2_{min} = 3.5 GeV^2. The green band includes experimental uncertainties on the fit.

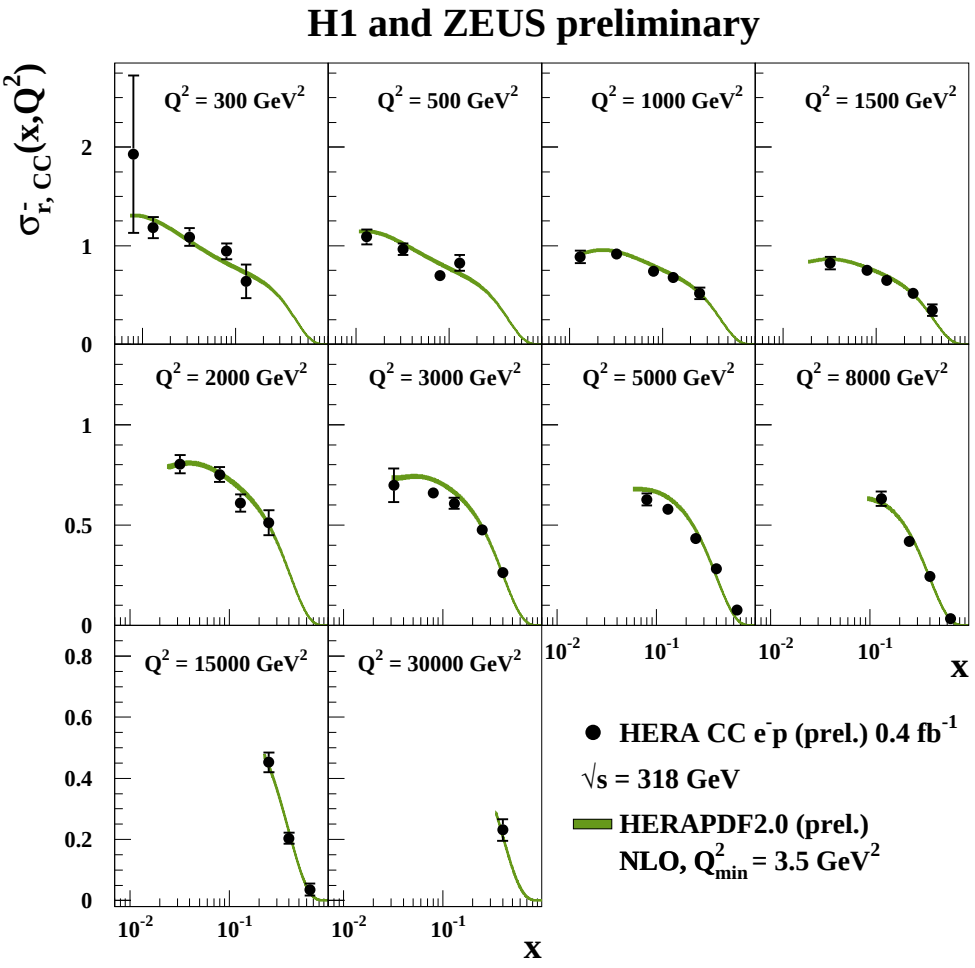

Figure 19: The combined HERA data for the inclusive CC $e^- p$ reduced cross section at $\sqrt{s}$ = 318 GeV compared to an NLO QCD fit with Q^2_{min} = 3.5 GeV^2. The green band includes experimental uncertainties on the fit.

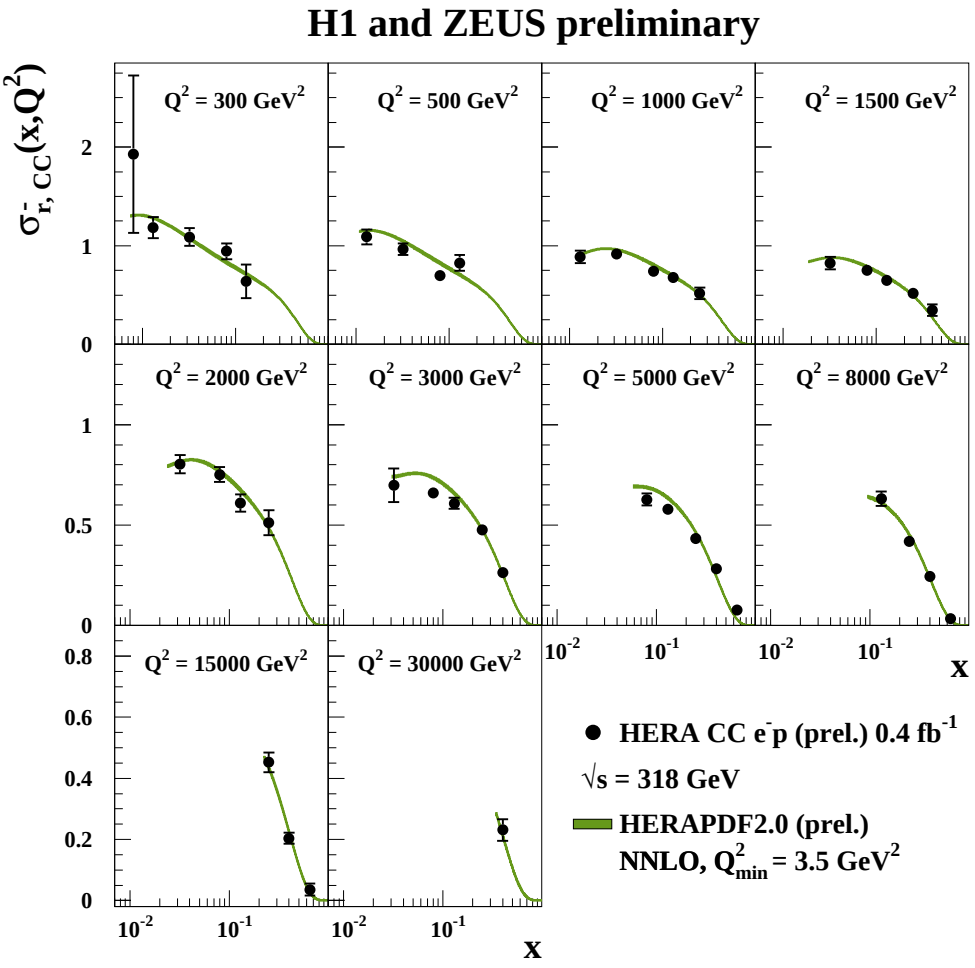

Figure 20: The combined HERA data for the inclusive CC $e^- p$ reduced cross section at $\sqrt{s}$ = 318 GeV compared to an NNLO QCD fit with Q^2_{min} = 3.5 GeV^2. The green band includes experimental uncertainties on the fit.

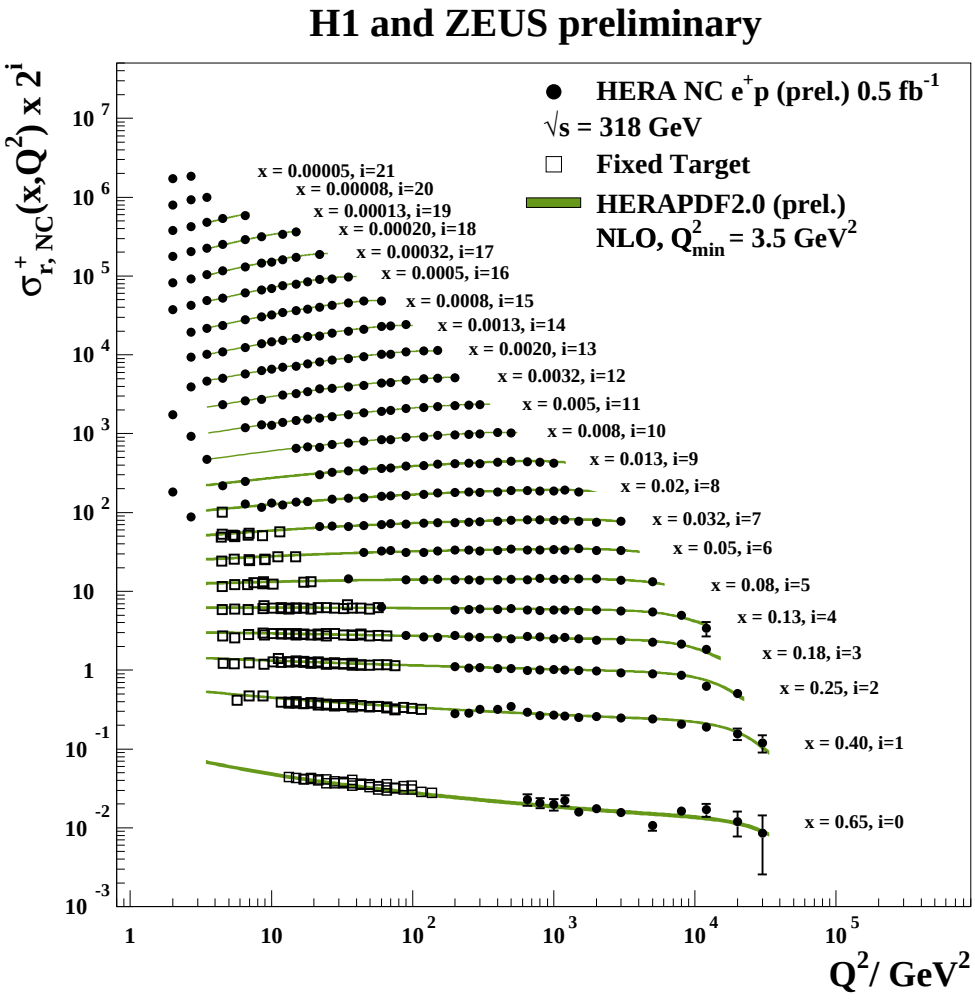

Figure 21: The combined HERA data for the inclusive NC e^+p reduced cross section and fixed target data compared to an NLO QCD fit with $Q^2_{min} = 3.5$ GeV^2. The green band includes experimental uncertainties on the fit.

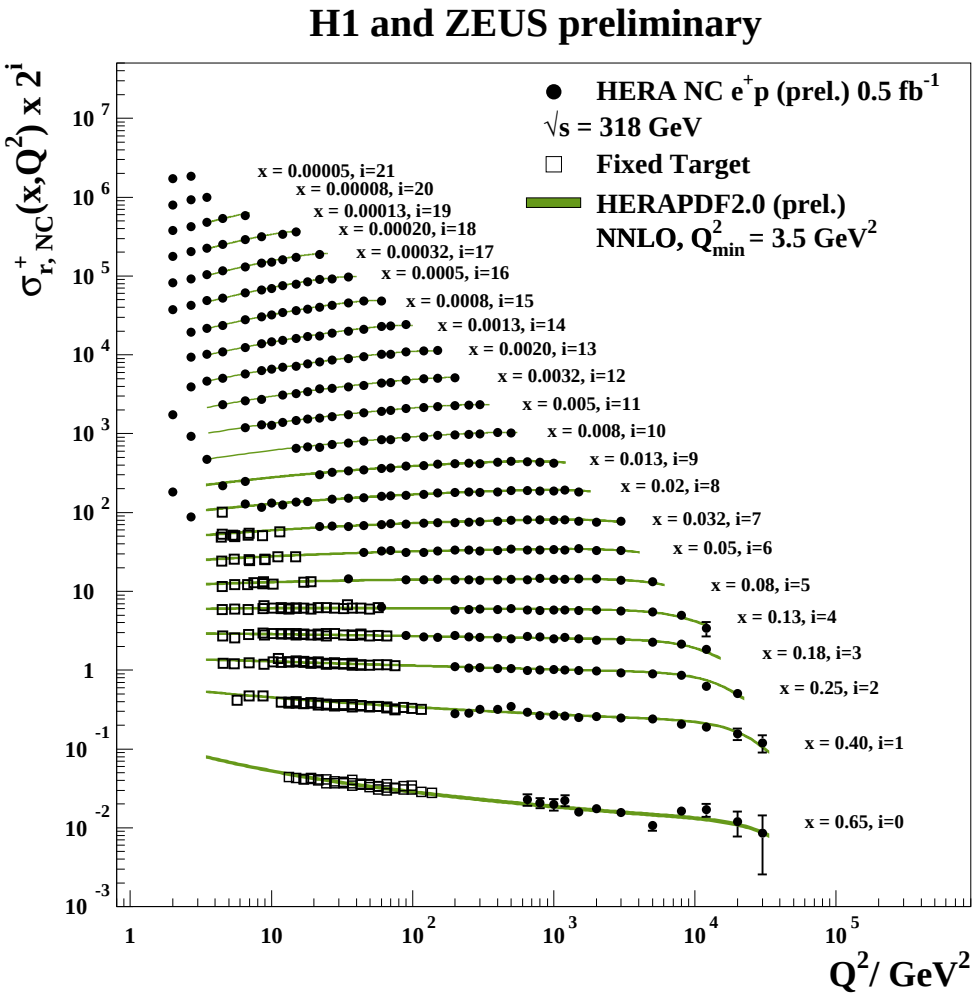

Figure 22: The combined HERA data for the inclusive NC e^+p reduced cross section and fixed target data compared to an NNLO QCD fit with $Q^2_{min} = 3.5$ GeV^2. The green band includes experimental uncertainties on the fit.

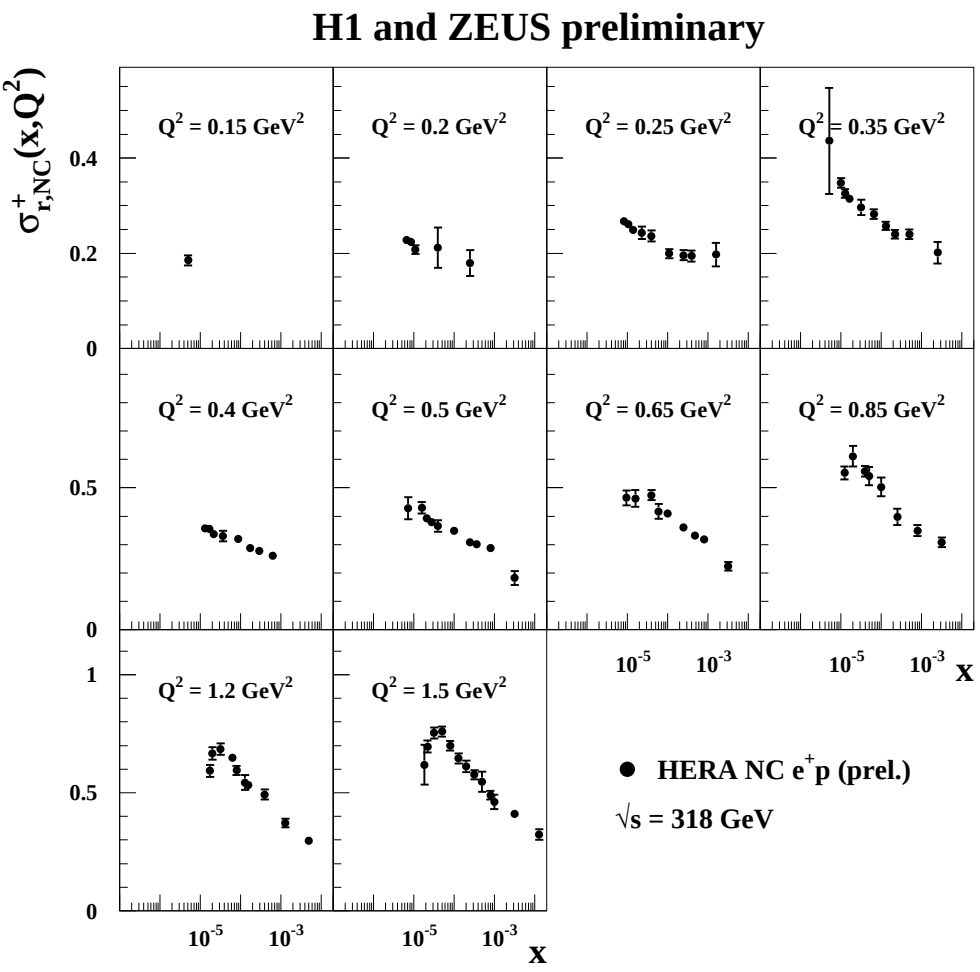

Figure 23: The combined HERA data for the inclusive NC e^+p reduced cross section at $\sqrt{s}$ = 318 GeV at very low Q^2.

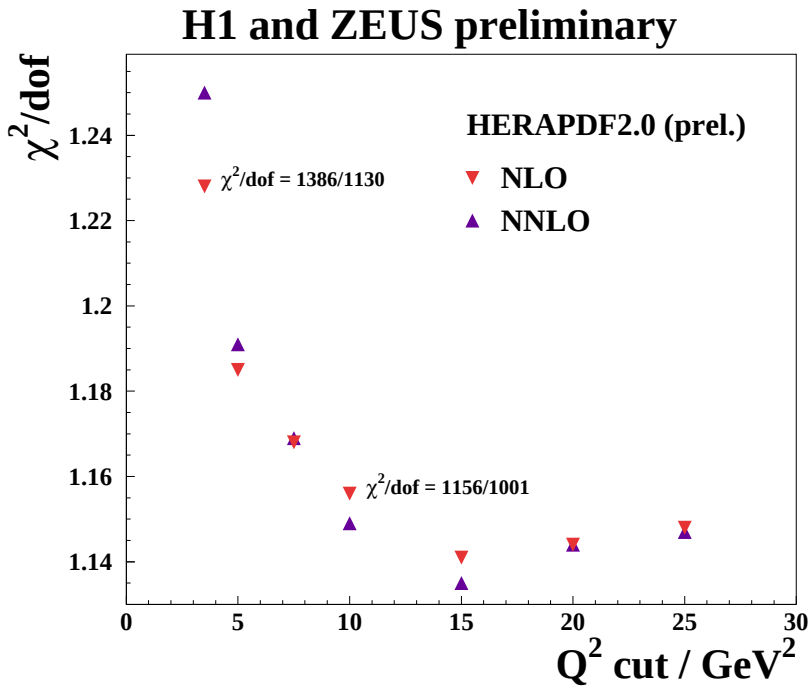

Figure 24: The χ^2 per degree of freedom vs the minimum Q^2 of data entering the QCD fit for the NLO and NNLO fits.

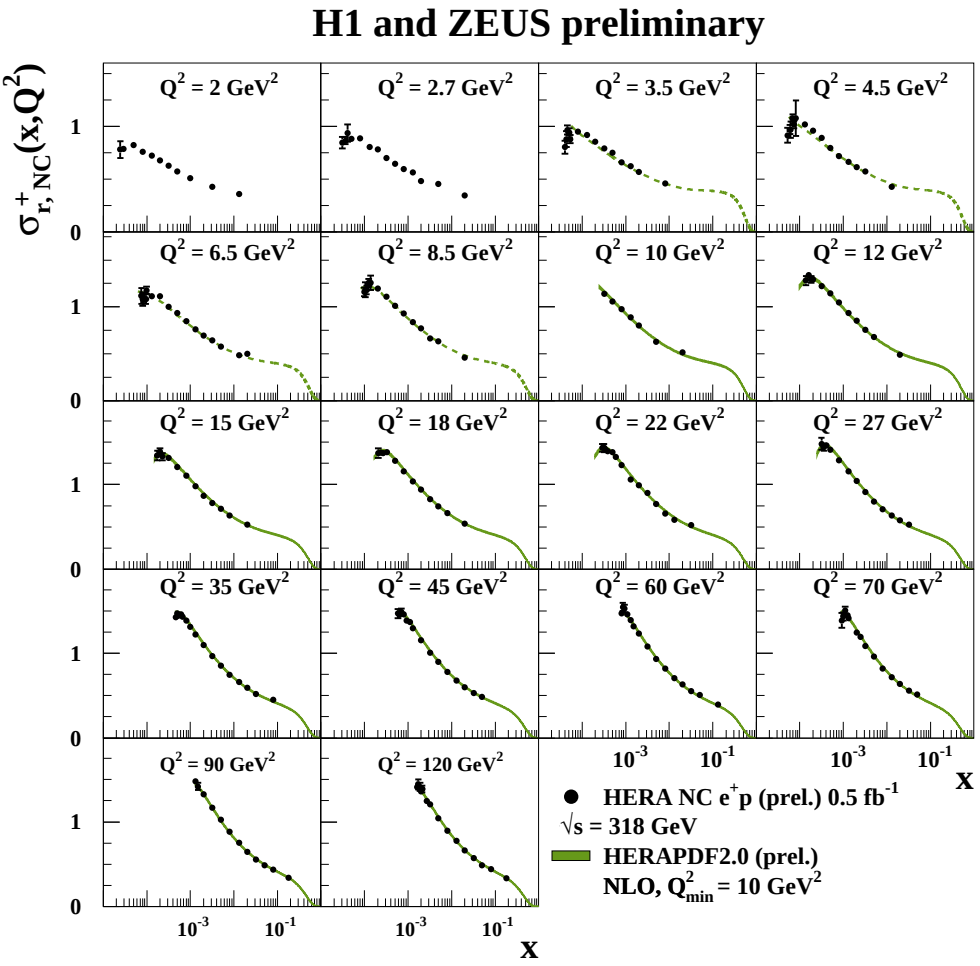

Figure 25: The combined low-Q^2 HERA data for the inclusive NC e^+p reduced cross section at $\sqrt{s}$ = 318 GeV compared to an NLO QCD fit with Q^2_{min} = 10 GeV^2. The green band includes experimental uncertainties on the fit.

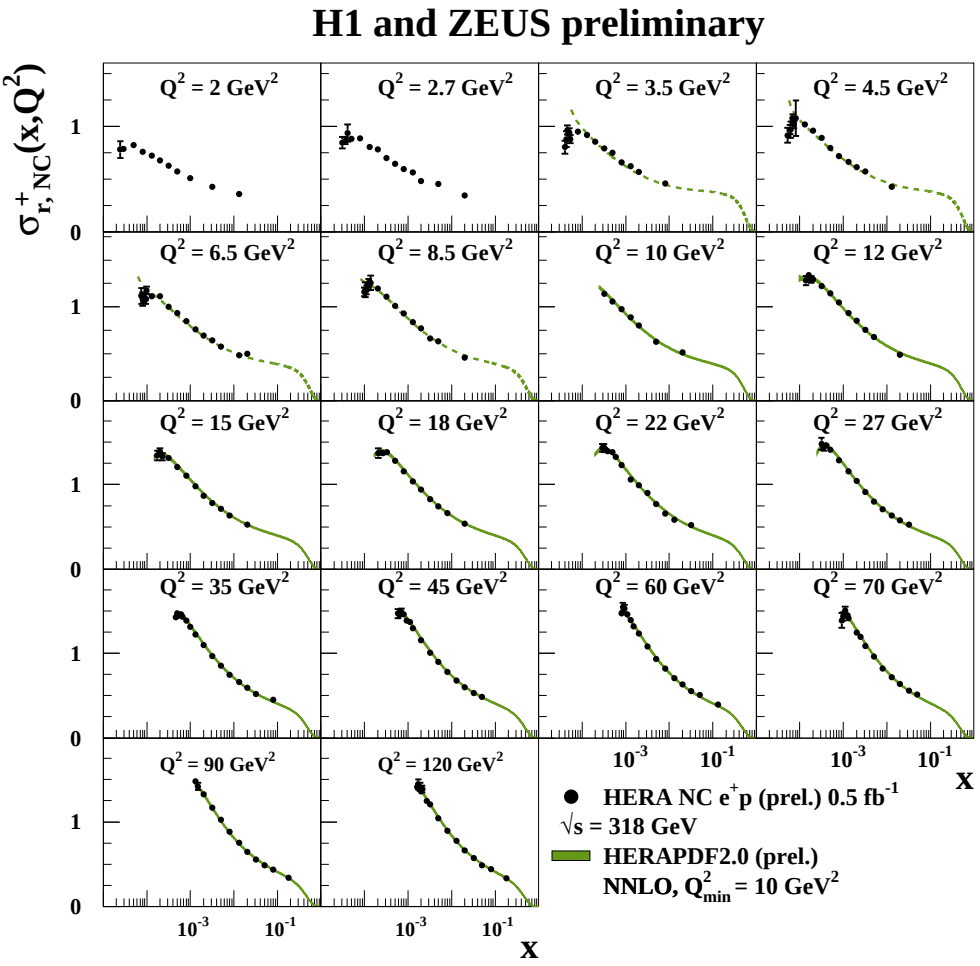

Figure 26: The combined low-Q^2 HERA data for the inclusive NC e^+p reduced cross section at $\sqrt{s}$ = 318 GeV compared to an NNLO QCD fit with Q^2_{min} = 10 GeV^2. The green band includes experimental uncertainties on the fit.

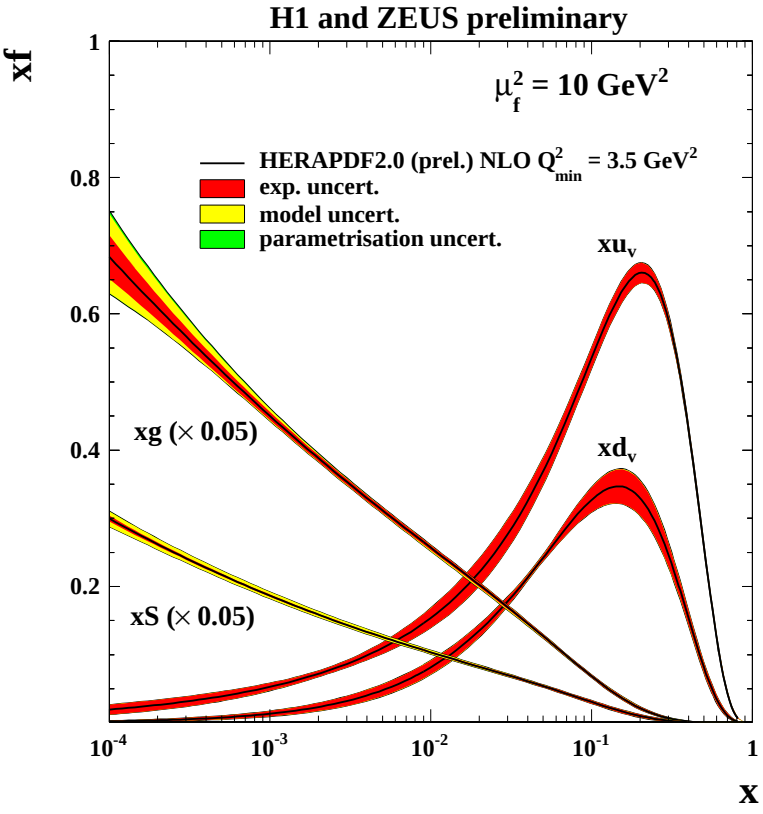

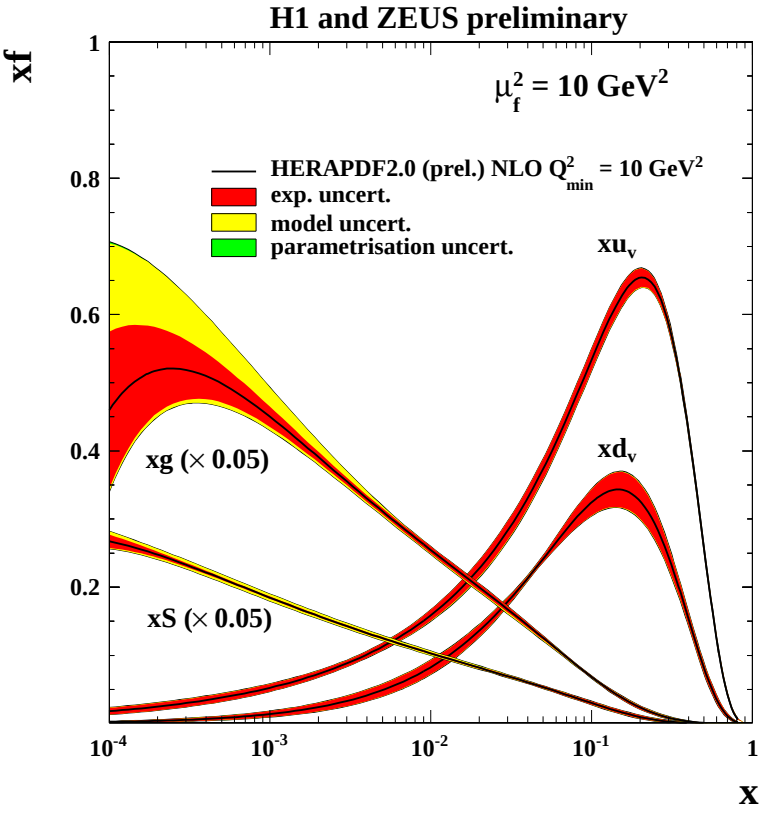

Figure 27: The parton distribution functions from HERAPDF2.0(prel.) at NLO, $xu_v, xd_v, xS = 2x(\bar{U} + \bar{D}), xg$, at the scale $\mu_f^2 = 10$ GeV^2, for the $Q^2_{min} = 3.5$ GeV^2 fit (top) and the $Q^2_{min} = 10$ GeV^2 fit (bottom) The gluon and sea distributions are scaled down by a factor 20. The experimental, model and parametrisation uncertainties are shown separately.

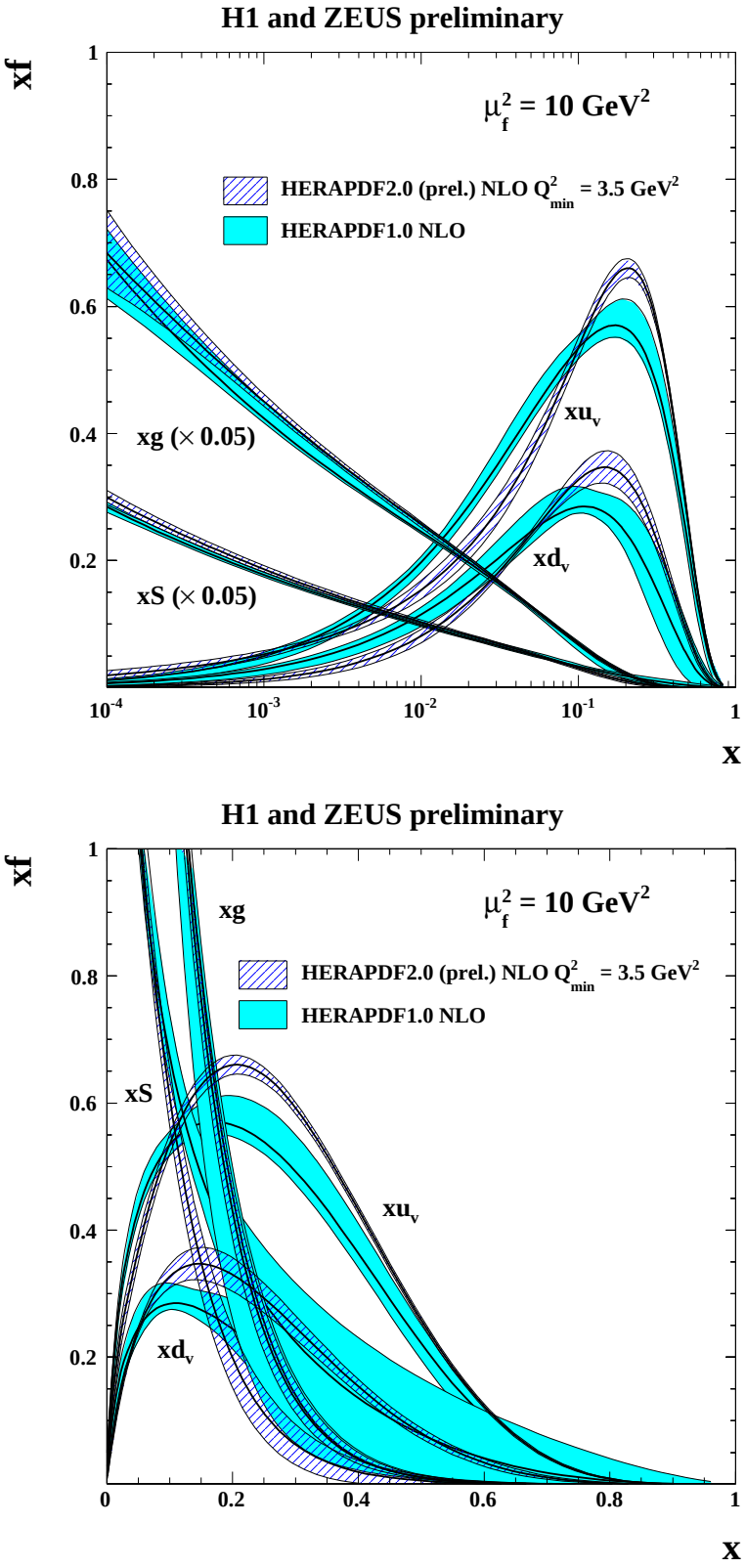

Figure 28: The parton distribution functions from HERAPDF2.0(prel.) at NLO, xu_v, xd_v, $xS = 2x(\bar{U} + \bar{D})$, xg, at the scale $\mu_f^2 = 10$ GeV^2, for the $Q^2_{min} = 3.5$ GeV^2 fit compared to HERAPDF1.0 on log (top) and linear (bottom) scales. The bands represent the total uncertainties.

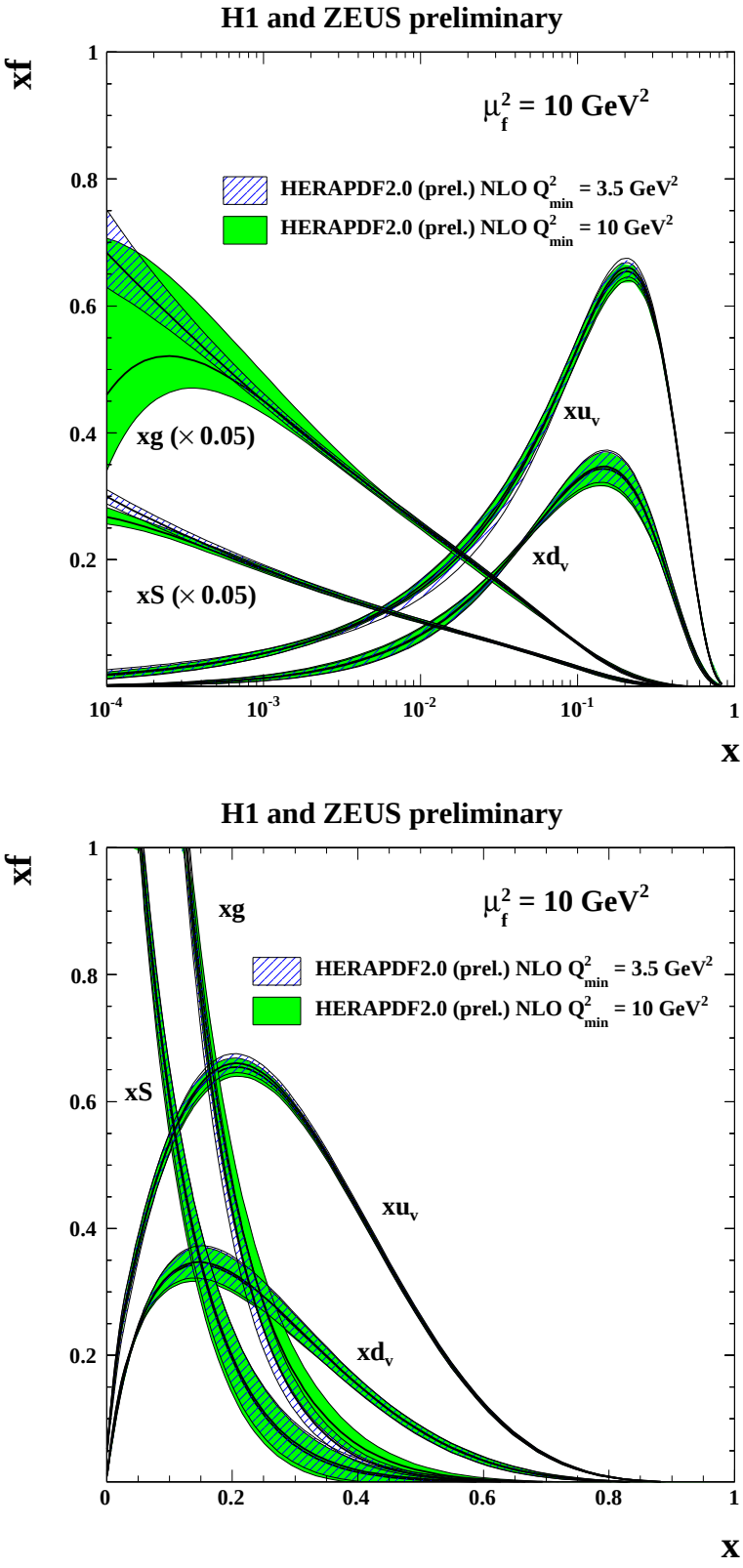

Figure 29: The parton distribution functions from HERAPDF2.0(prel.) at NLO, xu_v, xd_v, $xS = 2x(\bar{U} + \bar{D})$, xg, at the scale $\mu_f^2 = 10$ GeV^2, for the $Q^2_{min} = 3.5$ GeV^2 fit compared to the $Q^2_{min} = 10$ GeV^2 fit on log (top) and linear (bottom) scales.. The bands represent the total uncertainties.

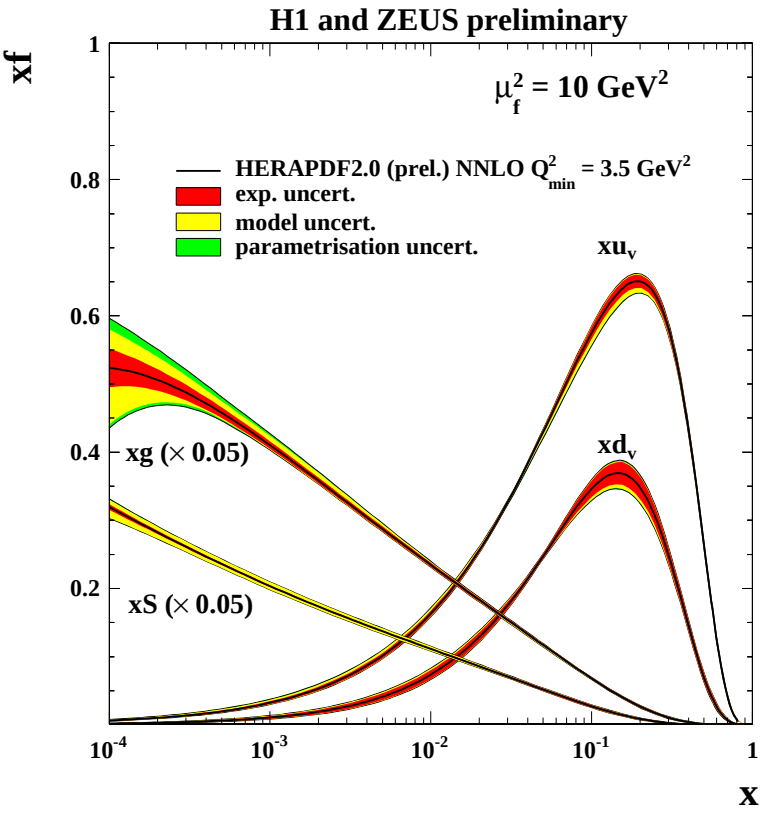

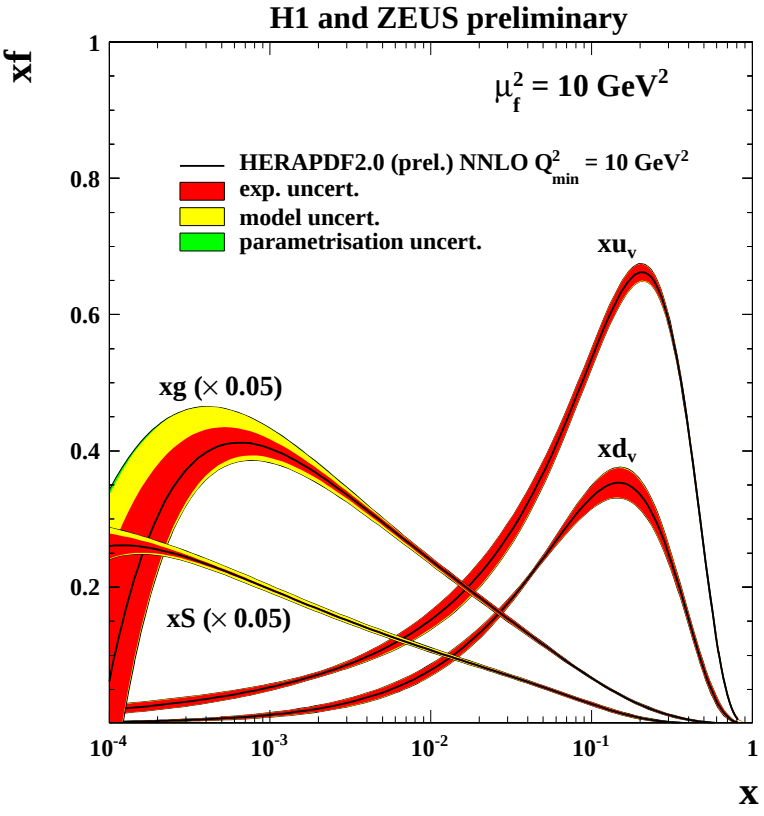

Figure 30: The parton distribution functions from HERAPDF2.0(prel.) at NNLO, $xu_v, xd_v, xS = 2x(\bar{U} + \bar{D}), xg$, at the scale $\mu_f^2 = 10$ GeV^2, for the $Q^2_{min} = 3.5$ GeV^2 fit (top) and the $Q^2_{min} = 10$ GeV^2 fit (bottom) The gluon and sea distributions are scaled down by a factor 20. The experimental, model and parametrisation uncertainties are shown separately.

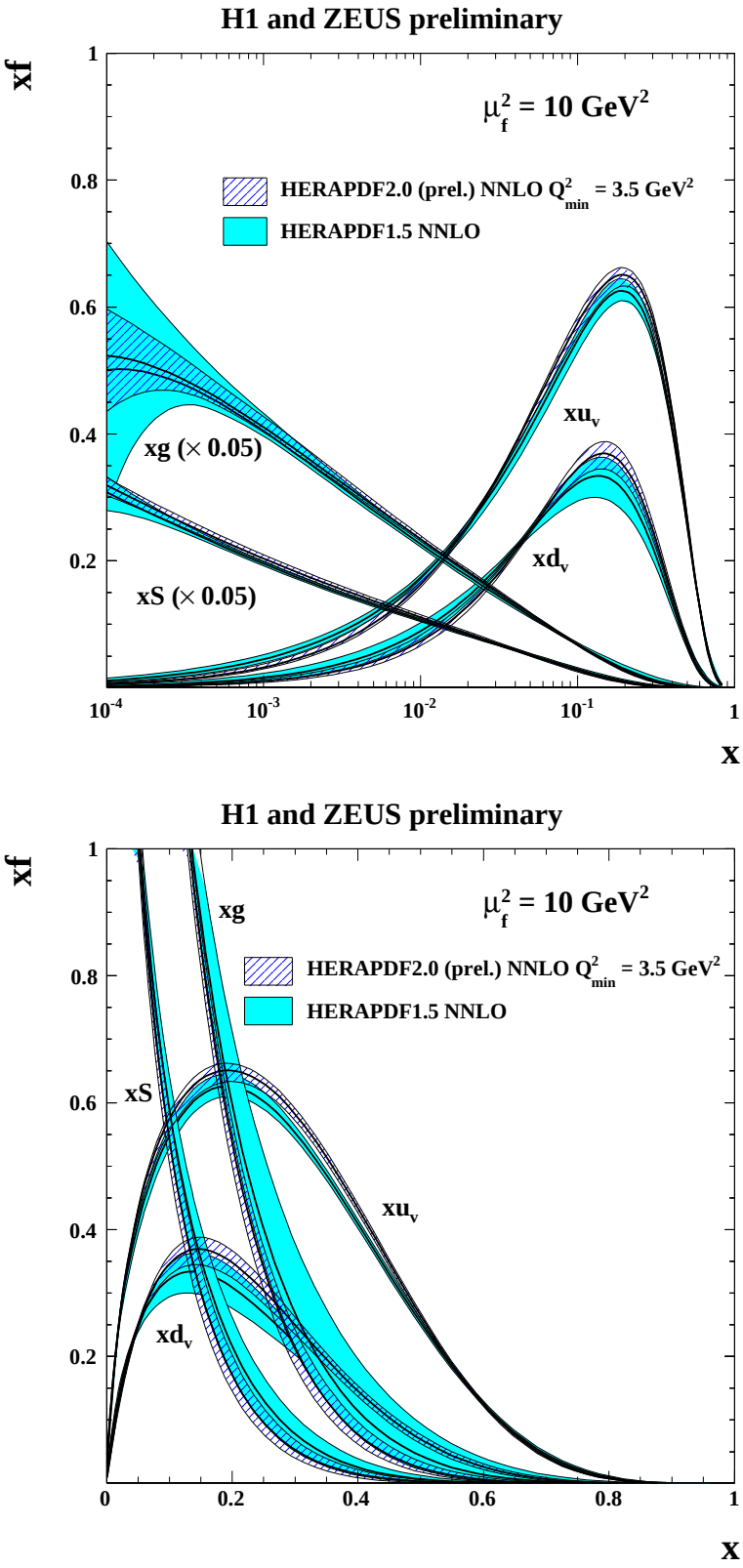

Figure 31: The parton distribution functions from HERAPDF2.0(prel.) at NNLO, $xu_v, xd_v, xS = 2x(\bar{U} + \bar{D}), xg$, at the scale $\mu_f^2 = 10$ GeV^2, for the $Q^2_{min} = 3.5$ GeV^2 fit compared to HERAPDF1.5 NNLO on log (top) and linear (bottom) scales. The bands represent the total uncertainties.

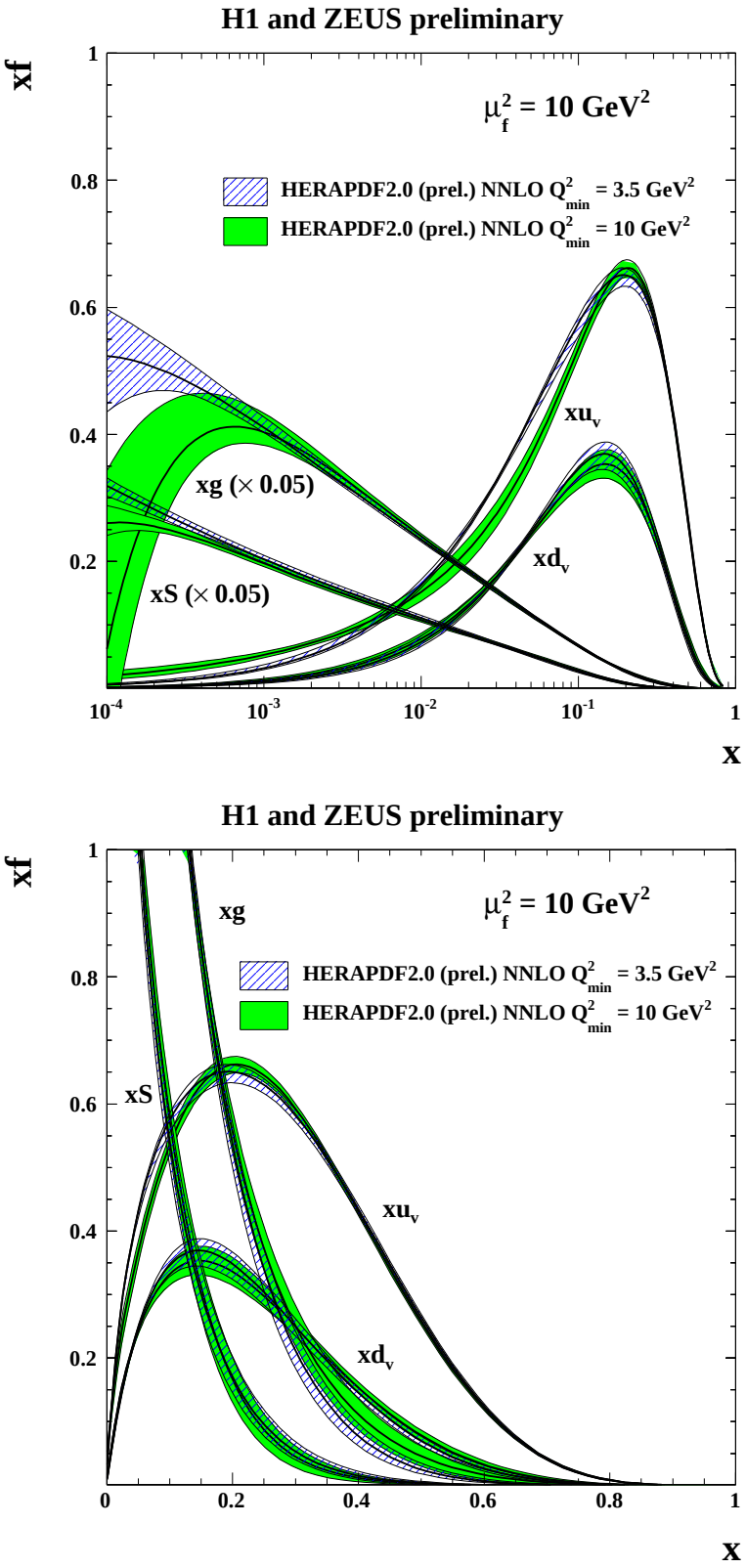

Figure 32: The parton distribution functions from HERAPDF2.0(prel.) at NNLO, $xu_v, xd_v, xS = 2x(\bar{U} + \bar{D}), xg$, at the scale $\mu_f^2 = 10$ GeV^2, for the $Q^2_{min} = 3.5$ GeV^2 fit compared to the $Q^2_{min} = 10$ GeV^2 fit on log (top) and linear (bottom) scales. The bands represent the total uncertainties.